Check for updates

JGR Earth Surface

RESEARCH ARTICLE
10.1029/2023JF007421

Characterizing Subglacial Hydrology Within the Amery Ice Shelf Catchment Using Numerical Modeling and Satellite Altimetry

Martin G. Wearing[1,2], Christine F. Dow[3], Daniel N. Goldberg[2], Noel Gourmelen[2], Anna E. Hogg[4], and Livia Jakob[5]

[1]Now at ESA Centre for Earth Observation, ESRIN, Rome, Italy, [2]School of Geosciences, University of Edinburgh, Edinburgh, UK, [3]Department of Geography and Environmental Management, University of Waterloo, Waterloo, ON, Canada, [4]School of Earth and Environment, University of Leeds, Leeds, UK, [5]Earthwave Ltd, Edinburgh, UK

Abstract Meltwater forms at the base of the Antarctic Ice Sheet due to geothermal heat flux (GHF) and basal frictional dissipation. Despite the relatively small volume, this water has a profound effect on ice-sheet dynamics. However, subglacial melting and hydrology in Antarctica remain highly uncertain, limiting our ability to assess their impact on ice-sheet dynamics. Here we examine subglacial hydrology within the Amery Ice Shelf catchment, East Antarctica, using the subglacial hydrology model GlaDS. We calculate subglacial melt rates using a higher-order ice-flow model and two GHF estimates. We find a catchment-wide melt rate of 7.03 Gt year^{-1} (standard deviation = 1.94 Gt year^{-1}), which is ≥50% greater than previous estimates. The contribution from basal dissipation is approximately 40% of that from GHF. However, beneath fast-flowing ice streams, basal dissipation is an order of magnitude larger than GHF, leading to a significant increase in channelized subglacial flux upstream of the grounding line. We validate GlaDS using high-resolution interferometric-swath radar altimetry, with which we detect active subglacial lakes and fine-scale ice-shelf basal melting. We find a network of subglacial channels that connects areas of deep subglacial water coincident with active subglacial lakes, and channelized discharge at the grounding line coinciding with enhanced ice-shelf basal melting. The concentrated discharge of meltwater provides 36% of the freshwater released into the ice-shelf cavity, in addition to ice-shelf basal melting. This suggests that ice-shelf basal melting is strongly influenced by subglacial hydrology and could be affected by future changes in subglacial discharge, such as lake drainage or channel rerouting.

Plain Language Summary Melting beneath the Antarctic Ice Sheet is relatively low, but the pattern of melting and meltwater drainage is important for controlling the flow of the overlying ice. Melting occurs due to geothermal heating from the underlying bedrock and heat generated from friction as the ice slides over the bedrock. Despite its importance, we know very little about melting beneath the Antarctic Ice Sheet. Here we use a numerical model to calculate meltwater drainage pathways beneath part of the ice sheet that flows into the Amery Ice Shelf, East Antarctica. We find that total melting is 7 gigatonnes per year. This is 50% more than previous studies because our model can resolve high melting beneath areas where the ice sheet is flowing fast. Using satellite observations of ice-sheet surface elevation change, we detect the filling and draining of lakes at the base of the ice sheet and ocean melting beneath the floating ice shelf. We use these observations to validate the modeled meltwater drainage pathways at the base of the ice sheet. These findings suggest that meltwater drainage from the base of the ice sheet may play an important role in controlling ocean melting of the floating ice shelf.

Key Points:

- We use the spatial distribution of ice-shelf basal melting and location of active subglacial lakes to validate a subglacial hydrology model
- Subglacial channels link subglacial lakes and focus meltwater discharge at the grounding line, triggering enhanced ice-shelf melting
- Modelled total subglacial melt is 7 Gt yr^{-1} and contributes 36% of the freshwater released in the ice-shelf cavity

Supporting Information:

Supporting Information may be found in the online version of this article.

Correspondence to:

M. G. Wearing,
mwearing@ed.ac.uk;
martin.wearing@esa.int

Citation:

Wearing, M. G., Dow, C. F., Goldberg, D. N., Gourmelen, N., Hogg, A. E., & Jakob, L. (2024). Characterizing subglacial hydrology within the Amery Ice Shelf catchment using numerical modeling and satellite altimetry. *Journal of Geophysical Research: Earth Surface*, *129*, e2023JF007421. https://doi.org/10.1029/2023JF007421

Received 31 AUG 2023
Accepted 15 MAR 2024

Author Contributions:

Conceptualization: Martin G. Wearing, Noel Gourmelen
Formal analysis: Martin G. Wearing
Funding acquisition: Noel Gourmelen
Investigation: Martin G. Wearing
Methodology: Martin G. Wearing, Christine F. Dow, Daniel N. Goldberg, Noel Gourmelen, Anna E. Hogg, Livia Jakob
Project administration: Noel Gourmelen
Writing – original draft: Martin G. Wearing

© 2024. The Authors.
This is an open access article under the terms of the Creative Commons Attribution License, which permits use, distribution and reproduction in any medium, provided the original work is properly cited.

1. Introduction

Meltwater forms at the base of the Antarctic Ice Sheet due to geothermal heat flux (GHF) and heat generated by frictional dissipation in areas of basal sliding. The melt rate is determined by the difference between these heat sources and the sink of heat conducted into the overlying ice. Subglacial melting is only a small component of Antarctica's total mass balance (approximately 3% of surface accumulation (Pattyn, 2010)), but melting and the subsequent subglacial hydrology play an important role in controlling the dynamics of the ice sheet (Alley, 1996; Hewitt, 2013; Joughin et al., 2003) and its interaction with the ocean (Gwyther et al., 2023; Nakayama et al., 2021; Wei et al., 2020). Despite their importance, subglacial melt rates and hydraulic conditions beneath the Antarctic Ice Sheet remain highly uncertain because of a lack of observations and constraints (Pattyn et al., 2016).

Writing – review & editing: Martin G. Wearing, Christine F. Dow, Daniel N. Goldberg, Noel Gourmelen

Estimates of GHF beneath the Antarctic Ice Sheet have large variability (Burton-Johnson et al., 2020). GHF estimates are derived using different methods (e.g., magnetically derived (Fox Maule et al., 2005; Martos et al., 2017) and seismically derived (Shapiro & Ritzwoller, 2004; Shen et al., 2020)) and are difficult to validate due to a lack of in-situ data. On average within the Amery Ice Shelf catchment (AmISC), the area of focus for this study, the two most recent estimates (Martos et al., 2017; Shen et al., 2020) differ by 16%. In areas of fast ice flow, such as ice streams, large contributions to subglacial melting result from basal frictional dissipation (Dow et al., 2020; Joughin et al., 2009). Understanding the spatial-distribution, magnitude and uncertainty attributable to each of these components is important for determining the input into the subglacial hydrological network and impact on ice dynamics.

Subglacial hydrology controls the distribution of meltwater at the base of the ice sheet, with drainage assumed to be through either a distributed or channelized system (e.g., Flowers, 2015). High subglacial water pressure is thought to correspond to lower basal friction, influencing the speed and extent of ice streams (Alley, 1996; Hewitt, 2013; Joughin et al., 2003). Subglacial meltwater may be temporarily stored within subglacial lakes, which have been observed to fill and drain, potentially influencing ice flow (Fricker et al., 2007; Smith et al., 2017; Stearns et al., 2008; Wright & Siegert, 2012). Furthermore, the discharge of subglacial meltwater into the ocean provides a flux of freshwater and nutrients, impacting marine biological productivity (Death et al., 2014; Herraiz-Borreguero et al., 2016; Twelves et al., 2021), ocean circulation and enhancing ice-shelf basal melting (Gwyther et al., 2023; Jenkins, 2011; Le Brocq et al., 2013; Wei et al., 2020) with the potential to reduce ice-shelf buttressing (e.g., Reese et al., 2018; Goldberg et al., 2019). Therefore, accurate information about subglacial hydrology is important for understanding both ice-sheet dynamics and ocean properties.

Observations of subglacial lakes (Livingstone et al., 2022) and radar reflectivity from the ice-sheet base (e.g., Schroeder et al., 2013, 2015) confirm the presence of water, but not the rate of melting or details of subglacial hydrology. Previous studies have calculated subglacial melt rates for the entire Antarctic Ice Sheet (Pattyn, 2010; Van Liefferinge & Pattyn, 2013), but were primarily focused on melt rates in the interior of the ice sheet, using the Shallow Ice Approximation with 5-km model resolution, which might not sufficiently simulate ice dynamics at the margins of the ice sheet. Similarly, Pittard et al. (2016) used 5-km resolution to calculate subglacial melt rates within the AmISC with the primary focus of evaluating catchment flow and geometry under different GHF conditions. More recently, Kang et al. (2022) used an offline-coupled ice-flow and thermal model to estimate subglacial melt rates within the Lambert Glacier and American Highland sections of the Amery Ice Shelf (AmIS) Catchment. Using six different GHF products and comparing the results with the locations of subglacial lakes detected from ice-penetrating radar (Wright & Siegert, 2012), they concluded that only estimates using GHF products from Li et al. (2021) and Martos et al. (2017) could produce basal melting in the vicinity of the most inland subglacial lakes. Using a similar modeling set-up, Dawson et al. (2022) considered the impact of a transition from frozen to thawed ice-sheet basal conditions on ice-sheet mass balance, implicitly considering the spatial distribution of frozen and temperate bed across the Antarctic Ice Sheet.

Advances in our understanding of subglacial hydrology have been possible through the fusion of observations and modeling. Le Brocq et al. (2013) used subglacial hydrology modeling to demonstrate that ice-shelf basal channels that intersect grounding lines are coincident with discharge of subglacial meltwater. Smith et al. (2017) used satellite-altimetry observations of subglacial lake activity beneath Thwaites Glacier and subglacial meltwater routing, to infer the filling rate for subglacial lakes. Dow et al. (2020) used radar specularity at the ice-bed interface, to assess the extent of the distributed component of subglacial hydrology within the Aurora Subglacial Basin. However, some of these studies used a uniform estimate of GHF (70 mW m^{-2} (Joughin et al., 2009; Smith et al., 2017) and 55 mW m^{-2} (Dow et al., 2020)), while Le Brocq et al. (2013) used meltwater input from an Antarctic-wide model (Pattyn, 2010).

Here we characterize the subglacial hydrology within the catchment of the Amery Ice Shelf (AmIS), East Antarctica using numerical modeling and remote-sensing observations. Using an advanced subglacial hydrology model, GlaDS, we simulate both the distributed and channelized drainage components within the subglacial catchment and validate the model using observations of active subglacial lakes and ice-shelf basal melting detected from interferometric-swath radar altimetry. Furthermore, we assess the contributions to subglacial melting from GHF, basal dissipation and englacial temperature, and examine the uncertainties associated with each component.

21699011, 2024, 4, Downloaded from https://agupubs.onlinelibrary.wiley.com/doi/10.1029/2023JF007421 by University Of Waterloo Dana Po, Wiley Online Library on [09/08/2024]. See the Terms and Conditions (https://onlinelibrary.wiley.com/terms-and-conditions) on Wiley Online Library for rules of use; OA articles are governed by the applicable Creative Commons License

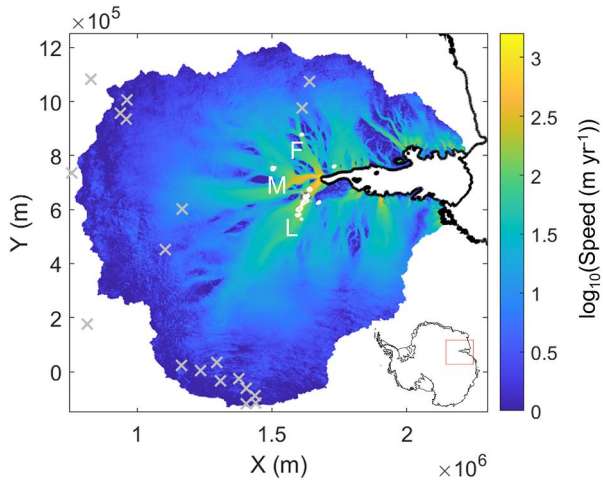


Figure 1. Extent of subglacial catchment draining into Amery Ice Shelf cavity. Ice surface speed (Rignot et al., 2017), shown with $\log_{10}$ colormap. Letters denote glaciers; Fisher (F), Mellor (M) and Lambert (L). The grounding line is shown in black (Depoorter et al., 2013). White outlines show active subglacial lakes detected by satellite altimetry. Gray crosses show subglacial lakes from inventory of Wright and Siegert (2012). Insert map shows location.

2. Study Area: Amery Ice Shelf Catchment (AmISC)

AmIS is the third largest ice shelf in Antarctica and drains a catchment of approximately 1.3×10^6 km^2 (Shepherd et al., 2019). AmIS is confined within a long and diverging embayment and is fed predominantly through a primary outlet at its southernmost point, where three ice streams converge: Fisher, Mellor and Lambert glaciers (Figure 1). The AmISC contributes 86 (±31) Gt year^{-1} of freshwater flux to the ocean from ice-shelf basal melting and iceberg calving (Rignot et al., 2013). The ice shelf provides buttressing to the upstream grounded ice (Fürst et al., 2016), although the stress regime in the downstream two thirds of the ice shelf make it potentially vulnerable to hydrofracture (Lai et al., 2020). An active subglacial lake has previously been detected beneath Lambert Glacier, approximately 100 km upstream of the grounding line (Siegfried & Fricker, 2018; Smith et al., 2009).

3. Methods

The main focus of this study is to assess the subglacial hydrology of the AmIS catchment. A key component of subglacial hydrology modeling is the rate and volume of meltwater input to the system. In order to establish the meltwater input we have to determine (a) the extent of the subglacial catchment, which may differ from the established ice-flow catchments, and (b) the distribution and magnitude of subglacial melting. Clues to the extent and activity of the subglacial hydrology system can be obtained from observations of active subglacial lakes and ice-shelf basal melting. We discuss the methods for obtaining these components before providing details of the subglacial hydrology modeling, which we validate using observations from interferometric-swath radar altimetry.

3.1. Calculating the Extent of the Subglacial Catchment

To determine the extent of the subglacial hydrological network draining into the AmIS ocean cavity, we estimate the hydraulic potential (ϕ (Pa)) assuming subglacial water pressure (p_w (Pa)) is equal to the ice overburden pressure (Shreve, 1972), such that

$$\phi = p_w + \rho_w g z = \rho_i g H + \rho_w g z, \tag{1}$$

where ρ_w (kg m^{-3}) and ρ_i (kg m^{-3}) are the density of water and ice respectively, g (m s^{-1}) is gravitational acceleration, H (m) is the ice-sheet thickness and z (m) is bed elevation. We use values of H and z from BedMachine Antarctica V2 (Morlighem et al., 2020) at 500-m resolution. We then use the MATLAB toolbox TopoToolbox (Schwanghart & Scherler, 2014) to determine the hydrological drainage pathways (Figure S1 in Supporting Information S1). The full catchment has a total area of 1.28×10^6 km^2. The maximum bounds of this area, plus an additional 80 km, delineates the rectangular domain considered in the ice-flow model (Section 3.2.2).

3.2. Calculating Subglacial Melt Rate

Subglacial melting results from the energy balance of GHF, basal frictional dissipation, and heat conducted into the overlying ice (Cuffey & Paterson, 2010). The melt rate, M (m s^{-1}), is given by

$$M = \frac{G + \tau_b u_b + k_i \theta_b}{L_i \rho_i}, \tag{2}$$

where: G (W m^{-2}) is the geothermal heat flux; τ_b (Pa) and u_b (m s^{-1}) are the basal shear stress and velocity, the product of which is frictional dissipation; k_i (W m^{-1} K^{-1}) is the thermal conductivity; θ_b (K m^{-1}) is the vertical gradient in basal ice temperature; L_i (kJ kg^{-1}) is the latent heat of ice; and ρ_i (kg m^{-3}) is the density of ice. Unlike in Greenland there is no input of meltwater from surface melting (Karlsson et al., 2021). The total catchment melt

21699011, 2024, 4, Downloaded from https://agupubs.onlinelibrary.wiley.com/doi/10.1029/2023JF007421 by University Of Waterloo Dana Po, Wiley Online Library on [09/08/2024]. See the Terms and Conditions (https://onlinelibrary.wiley.com/terms-and-conditions) on Wiley Online Library for rules of use; OA articles are governed by the applicable Creative Commons License

21699011, 2024, 4, Downloaded from https://agupubs.onlinelibrary.wiley.com/doi/10.1029/2023JF007421 by University Of Waterloo Dana Po, Wiley Online Library on [09/08/2024]. See the Terms and Conditions (https://onlinelibrary.wiley.com/terms-and-conditions) on Wiley Online Library for rules of use; OA articles are governed by the applicable Creative Commons License

rate is calculated by integrating the melt rate over the extent of the subglacial catchment determined in Section 3.1.

One approach to calculating the subglacial melt rate would be to run a thermo-mechanical ice-sheet model, with GHF as a basal boundary condition (e.g., Dawson et al., 2022; Kang et al., 2022; Karlsson et al., 2021; Seroussi et al., 2017). However, the approach could encounter a number of problems. First, the model would need to be spun-up over centuries/millennia in order to ensure the englacial temperature reaches equilibrium. Assuming that the present day geometry and climatic conditions are used, this would fail to account for any temporal changes in surface mass balance, air temperature and geometry during that time. Furthermore, it would be difficult to specify unknown parameters such as basal sliding and ice strength, which are usually inferred with an ice-sheet model inversion, and may require constraints on englacial temperature to ensure the problem is not ill-posed (see Section 3.2.2). We take an alternative approach and instead determine each term in Equation 2 separately and assess the uncertainties associated with each term.

3.2.1. Geothermal Heat Flux

GHF in Antarctica is poorly constrained (Burton-Johnson et al., 2020). Although a number of GHF products exist, here we use the two most recent estimates, which use contrasting methods, magnetically derived: Martos GHF (Martos et al., 2017), and seismically derived: Shen GHF (Shen et al., 2020). Hereafter we refer to these estimates as Martos GHF and Shen GHF. Within the AmISC, these two GHF products broadly cover the range of GHF values suggested by other previous studies (Burton-Johnson et al., 2020). Both Martos and Shen GHF products are provided at 15-km spatial resolution. We account for changes in GHF due to local topography following Colgan et al. (2021), first linearly interpolating to a 500-m grid and then using bed topography from BedMachine Antarctica V2 (Morlighem et al., 2020). This increases GHF where the bed is deep and decreases GHF where the bed is shallow, with a maximum absolute change of 100 mW m^{-2}, although the average GHF within the AmISC remains unchanged (<0.05%; Table S1 and Figure S2 in Supporting Information S1). This approach ensures that the relatively coarse resolution GHF products are sampled at the scale of the subglacial hydrology modeling, and that subglacial meltwater from GHF is routed correctly, particularly at the boundaries between subglacial catchments.

Both GHF products come with associated spatial-varying uncertainty values. The Martos GHF provides a range of uncertainty, while the Shen GHF provides a standard deviation (SD) (Figure S3 in Supporting Information S1). Assuming the Martos and Shen GHF estimates are equally likely, we assess the total uncertainty in the catchment-wide GHF by randomly sampling each distribution 1,000 times; applying the same proportion of uncertainty across the whole catchment, and integrating across the catchment to compute total GHF (see Text S1.2.2 in Supporting Information S1). We consider the Martos GHF values to be uniformly distributed with a range equal to the uncertainty value, and the Shen GHF values to be normally distributed with a SD equal to the uncertainty value. The two sets of random samples are then combined allowing a mean and SD to be calculated from the 2,000 samples (see Text S1.2.2 in Supporting Information S1). This approach implicitly assumes that the uncertainty in GHF is spatially correlated across the catchment, which is unlikely to be the case, and therefore provides a conservative estimate of uncertainty.

3.2.2. Basal Frictional Dissipation: Ice-Sheet Model Inversion

The flow of ice within the AmISC is simulated using the higher-order ice-flow model STREAMICE (Goldberg, 2011), with bed topography and ice thickness from BedMachine Antarctica V2 (Morlighem et al., 2020). A model inversion is used to assimilate observations of ice surface velocity (MEaSUREs InSAR-Based Antarctica Ice Velocity Map, Version 2 (Rignot et al., 2017)), with the basal friction (β^2) and ice stiffness (B) parameters inferred via an adjoint method (Goldberg & Sergienko, 2011). We assume the ice stiffness parameter is vertically uniform and calculate an initial guess (B_0) using the relationship between temperature and the rate factor, A, in Glen's Flow Law (Cuffey & Paterson, 2010, Equation 3.35; assuming $n = 3$).

$$B_0 = \frac{1}{2}A^{-\frac{1}{3}} \tag{3}$$

21699011, 2024, 4, Downloaded from https://agupubs.onlinelibrary.wiley.com/doi/10.1029/2023JF007421 by University Of Waterloo Dana Po, Wiley Online Library on [09/08/2024]. See the Terms and Conditions (https://onlinelibrary.wiley.com/terms-and-conditions) on Wiley Online Library for rules of use; OA articles are governed by the applicable Creative Commons License

We use the vertically averaged englacial temperature, which is calculated from the vertically distributed temperature estimate for grounded ice from Van Liefferinge and Pattyn (2013). In the ice shelf, our initial guess for ice stiffness (B_0) corresponds to an englacial temperature of −16°C.

During the inversion a cost function is minimized with β and B as control variables. We use a cost function that incorporates both the absolute and normalized misfit of the modeled to observed surface velocities,

$$J = \sum_i \frac{(u_{\mathrm{mod},i} - u_{obs,i})^2 + (v_{\mathrm{mod},i} - v_{obs,i})^2}{2N(1 + u_{err,i})^2} + \sum_i \frac{10^2\left((u_{\mathrm{mod},i} - u_{obs,i})^2 + (v_{\mathrm{mod},i} - v_{obs,i})^2\right)}{2N(u_{err,i}^2 + u_{obs,i}^2 + v_{obs,i}^2)} + \lambda_{B_0}\sum_i (B_i - B_{0,i})^2 + \lambda_\beta \sum_i (\nabla\beta_i)^2 + \lambda_B \sum_i (\nabla B_i)^2, \quad (4)$$

where $u_{\mathrm{mod},i}$, $v_{\mathrm{mod},i}$ and $u_{obs,i}$, $v_{obs,i}$ are the modeled and observed surface velocity components in cell i, and $u_{err,i}$ is the associated observational error (Rignot et al., 2017). N is the total number of ice covered cells. The first and second terms on the right hand side of Equation 4 are the absolute and normalized misfit between the modeled and observed surface velocities respectively. By using both of these terms we ensure the inversion is optimized in both fast and slow flowing regions. This is important to ensure the correct representation of ice flow and critically, basal dissipation, throughout the domain. The final three terms in Equation 4 are regularization terms. The first of these limits the degree to which the ice stiffness parameter (B_i) can differ from the initial guess ($B_{0,i}$), while the final two terms limit unphysically large spatial gradients in basal friction and ice stiffness parameters. The regularization terms are kept constant ($\lambda_\beta = \lambda_B = 0.1 \times 10^5$ and $\lambda_{B_0} = 0.1 \times 10^{-2}$ where ice is grounded, and $\lambda_{B_0} = 0$ where ice is floating; values are based on the 2D L-surface analysis of Goldberg et al. (2019)). With two unknown parameters this problem is inherently ill-posed, however by limiting the degree to which ice stiffness can vary away from the initial value this problem is more thoroughly constrained.

To minimize the cost function an adjoint approach is followed using the automatic differentiation tool OpenAD (Utke et al., 2008), which identifies the sensitivity of the cost function to changing the values of B and β. We use this inversion process to calculate the basal frictional dissipation, which is the product of basal shear stress (τ_b) and basal velocity (u_b). The optimized parameters are obtained following 500 iterations of the inversion.

We run the inversion twice from the same initial conditions with 2 and 5-km rectangular grid spacing, obtaining values for τ_b and u_b. The results are then linearly interpolated to a common grid (500-m; BedMachine Antarctica V2) to calculate melt rate.

It is difficult to quantify the uncertainty in the assimilated basal shear stress and velocity as these quantities are inferred via optimization of the ice-sheet model to match observations. We therefore use the uncertainty in surface velocity as a proxy for the uncertainty in basal motion. We neglect uncertainty in shear stress arising from the basal friction parameter, as estimating parametric uncertainty conditioned on observations involves sophisticated computation which is beyond the scope of this study (Isaac et al., 2015; Recinos et al., 2023). The surface velocity product provides standard deviations for both the x and y components (Figure S4 in Supporting Information S1). We apply this uncertainty directly to the inferred basal velocity. In a similar manner to the previous section, we calculate the catchment-wide contribution to melting from basal dissipation by considering 1,000 realizations, which randomly sample the normally distributed uncertainties, applying the same proportion of uncertainty across the catchment, with independent sampling of the x and y components (see Text S1.3.1 in Supporting Information S1).

3.2.3. Englacial Temperature

In a similar manner to Joughin et al. (2009), we prescribe ice-sheet englacial temperature based on an independent model estimate rather than coupling a thermo-mechanical model to our dynamical ice-flow model (examples of coupled models include; Karlsson et al., 2021; Seroussi et al., 2017). We use model results from Van Liefferinge and Pattyn (2013), who used an ensemble of runs that incorporate multiple GHF estimates adjusted to account for the presence of known subglacial lakes (Figure 1). Using this result we determine: (a) the depth-averaged

englacial temperature, which is used to provide an initial estimate of ice stiffness (B_0; Section 3.2.2); and (b) the vertical gradient in temperature at the ice base, which is used to calculate the vertical heat conduction term in the energy balance (Equation 2). The vertical gradient in englacial temperature at the ice base is linearly interpolated to the BedMachine grid with 500-m spacing.

To assess uncertainty in the basal temperature gradient, and to capture potential inconsistency when using GHF estimates that are different from those used by Van Liefferinge and Pattyn (2013), we estimate the basal temperature gradient using the two GHF products. We use the analytical solution for the steady-state vertical englacial temperature profile, assuming no horizontal advection and a frozen bed, following Robin (1955) (Text S1.4 in Supporting Information S1). We use surface accumulation and temperature from regional climate model RACMO2.3p2 (van Wessem et al., 2018), and ice thickness from BedMachine Antarctica V2 (Morlighem et al., 2020), calculating englacial temperature for both the Martos and Shen GHF. We then calculate the vertical gradient in temperature at the ice base, neglecting areas where the analytical solution suggests the basal temperature is greater than the freezing point (Figure S5 in Supporting Information S1). This produces average temperature gradients of -0.0241 K m^{-1} (Martos; SD = 0.0039 K m^{-1}) and -0.0208 K m^{-1} (Shen; SD = 0.0089 K m^{-1}). When compared with the basal temperature gradient from Van Liefferinge and Pattyn (2013) (mean = -0.0140 K m^{-1}, SD = 0.0103 K m^{-1}), the average difference is 0.0085 K m^{-1}. Acknowledging the limitations of the analytical solution (no horizontal advection, frozen bed), and the difference with the Van Liefferinge and Pattyn (2013) result, we consider a conservative representation of the uncertainty for the value of vertical temperature gradient, which is normally distributed with a SD of 0.01 K m^{-1} about the vertical temperature gradient from Van Liefferinge and Pattyn (2013). Again we perform 1,000 realizations sampling randomly from this distribution.

3.3. Observations From Interferometric-Swath Radar Altimetry

Observations of active subglacial lakes and ice-shelf basal melting, obtained from interferometric-swath radar altimetry, provide insight into the nature of the subglacial hydrology system.

3.3.1. Active Subglacial Lakes

We detect the location and outline of active subglacial lakes from CryoSat-2 interferometric-swath radar altimetry acquired from 2010 to 2020, using the method of Malczyk et al. (2020). Subglacial lake masks are defined as regions with significant localized elevation change ($\geq$0.5 m year^{-1}) relative to the background elevation change.

3.3.2. Ice-Shelf Basal Melting

We calculate submarine melt rates beneath the AmIS using the mass conservation approach (Gourmelen et al., 2017). We produce Lagrangian rates of surface elevation change from CryoSat-2 interferometric-swath radar altimetry acquired from 2010 to 2020 (Gourmelen et al., 2018), and corresponding ice velocity from the ITS_LIVE data set (Gardner et al., 2019). We calculate ice divergence using ice velocity and BedMachine Antarctica V2 ice-shelf thickness (Morlighem et al., 2020), with surface mass balance and firn densification from RACMO2.3p2 (van Wessem et al., 2018). The basal melt rate uncertainty accounts for each of the mass conservation terms as described in Adusumilli et al. (2020). To remove erroneous melt rate values associated with the advection of fractures near the ice-shelf front and fracture formation in shear margins, we apply a threshold whereby: (a) all melt rate values less than -9 m year^{-1} (i.e., unrealistic freeze-on); and (b) all melt rate values where shear rates exceed 0.03 years year^{-1} (i.e., identifying damaged shear margins (Wearing et al., 2015)), are removed. We then apply a single iteration of median filtering and median filling with a kernel size of 2.5×2.5 km, which reduces noise but maintains spatial details in melt rates.

3.4. Simulating Subglacial Hydrology

We use a hierarchy of subglacial hydrology models of differing complexity. First, we employ a subglacial routing approximation to investigate the influence of different melt rate components on the subglacial hydrology. Second, we use a more sophisticated and physically realistic model that simulates both the channelized and distributed components of the subglacial drainage system, which we constrain with remote-sensing observations.

21699011, 2024, 4, Downloaded from https://agupubs.onlinelibrary.wiley.com/doi/10.1029/2023JF007421 by University Of Waterloo Dana Po, Wiley Online Library on [09/08/2024]. See the Terms and Conditions (https://onlinelibrary.wiley.com/terms-and-conditions) on Wiley Online Library for rules of use; OA articles are governed by the applicable Creative Commons License

21699011, 2024, 4, Downloaded from https://agupubs.onlinelibrary.wiley.com/doi/10.1029/2023JF007421 by University Of Waterloo Dana Po, Wiley Online Library on [09/08/2024]. See the Terms and Conditions (https://onlinelibrary.wiley.com/terms-and-conditions) on Wiley Online Library for rules of use; OA articles are governed by the applicable Creative Commons License

3.4.1. Meltwater Routing

We calculate routing according to an approximate subglacial hydraulic potential, where subglacial water pressure is assumed to be equal to the ice overburden pressure (Shreve, 1972). This is implemented using TopoToolbox (Schwanghart & Scherler, 2014), with filling of sinks within the hydraulic potential and single-direction flow routing. Once subglacial hydraulic pathways have been determined, the accumulated meltwater flux is then calculated by instantaneously routing meltwater along subglacial pathways. We calculated the accumulated meltwater flux from: the total melt rate, basal dissipation component only, and total melt rate with Martos and Shen GHF. When analyzing the contribution to the subglacial flux from basal dissipation, and assessing the difference between the two GHF estimates, we consider the relative contribution by normalizing the flux along the subglacial pathways with the flux when the total melt rate is used (i.e., a value of 0.5 indicates that 50% of the meltwater results from basal dissipation).

3.4.2. Modeling Distributed and Channelized Drainage Using GlaDS

We use the subglacial hydrology model GlaDS (Werder et al., 2013) to simulate the flow of meltwater at the ice base. This finite-element model considers water flow through a coupled system of distributed and channelized drainage elements, where channels are able to naturally develop, expand and contract. It uses an unstructured triangular mesh and is refined in regions where basal sliding is greater than 25 m $year^{-1}$. The minimum edge length is 700 m extending up to 16 km in the unrefined higher regions of the domain. The model is run to near steady state, in this case with a change in total channel discharge of $<5 \times 10^{-6}$ m^3 s^{-1} (Figure S6 in Supporting Information S1). Complete steady state could not be achieved due to some cyclical behavior observed in some of the channel segments with competition between channel growth from melt due to water flow, and channel closure from hydrostatic pressure.

Ice-sheet thickness and bed topography data are from BedMachine Antarctica V2 (Morlighem et al., 2020). To avoid instabilities in subglacial hydrology where there are areas of exposed bedrock (nunataks) or ice of less than 100 m thickness, these areas are assigned a minimum ice thickness of 100 m. This leads to a more stable drainage system, but the formation of an anomalously large channel in the vicinity of Jetty Peninsula on the western margin of AmIS, where there is a large area of exposed bedrock and the topography has been altered significantly. We do not expect such a large channel to form here and conclude that this is a result of the modified topography. To denote this we shade this area with a transparent gray box in the results figures.

The parameter choices in GlaDS closely follow previous studies (Dow, Karlsson, & Werder, 2018; Dow et al., 2020; Wei et al., 2020). The sheet conductivity is set to 1×10^{-4} $m^{7/4}$ $kg^{-1/2}$ after initial tests showed a lack of system pressurization at 1×10^{-3} $m^{7/4}$ $kg^{-1/2}$, and over pressurization and a lack of convergence with 1×10^{-5} $m^{7/4}$ $kg^{-1/2}$. The basal cavity height is 0.08 m.

GlaDS is run with high (1×10^{-2} $m^{3/2}$ $kg^{-1/2}$) and low (1×10^{-3} $m^{3/2}$ $kg^{-1/2}$) channel conductivity values. Previous GlaDS studies have used the value 5×10^{-2} $m^{3/2}$ $kg^{-1/2}$ but this was found to be unstable in application to this model domain due to regions of significant steep hydraulic potential in the primary troughs, beneath Fisher, Mellor and Lambert glaciers, that drove runaway channel growth when a higher channel conductivity was applied.

Furthermore, initial simulations saw anomalously high channel growth along isolated channel segments with channel cross-sectional area exceeding 1,000 m^2 (Figure S7 in Supporting Information S1). This channel growth is the result of frictional dissipation of meltwater flowing in channels and also leads to an increase in meltwater flux. At the main subglacial outlet this leads to a 30 m^3 s^{-1} increase in discharge (Figure S7 in Supporting Information S1). To address this unphysical channel growth, we cap channel cross-sectional area at 500 m^2 (Figures S6 and S7 in Supporting Information S1). Further investigation is needed to assess the contribution to subglacial discharge from frictional dissipation. However, capping channel cross-sectional area has little effect on channel locations, effective pressure or subglacial water depth (Figure S7 in Supporting Information S1).

4. Results

We first present our newly calculated subglacial melt rates and the observations from interferometric-swath radar altimetry, followed by the results of the subglacial hydrology modeling.

4.1. Subglacial Melt Rate

Geothermal heat flux values vary between 50 and 100 mW m^{-2} across the catchment, with the highest values generally found in the regions bordering the ice shelf (Figure 2a). Across the entire AmISC the total GHF is 7.02×10^{10} W (SD = 1.06×10^{10} W). The Martos GHF product suggests a 16% larger total GHF in comparison to the Shen product (Table S2 in Supporting Information S1). The largest differences in GHF are found near the southernmost part of the grounding line and at the downstream western margin of the ice shelf (Figure S8 in Supporting Information S1). In both locations the Martos GHF is up to 50 mW m^{-2} greater than the Shen GHF.

Both 2 and 5-km model inversions reproduce the observed surface velocities relatively well (Figure S9 and Table S3 in Supporting Information S1), with average misfits of −0.63 m $year^{-1}$ (SD = 5.04 m $year^{-1}$) and −0.78 m $year^{-1}$ (SD = 7.42 m $year^{-1}$) respectively. The 5-km inversion performs less well where there are large spatial gradients in flow speed, such as in the narrow tributary glaciers (Figure S9 in Supporting Information S1). When the model resolution is increased further to 1-km, to test convergence, the inversion results are improved marginally (Figure S10 and Table S4 in Supporting Information S1).

Heat produced from basal dissipation increases with ice-flow speed, with negligible basal dissipation in the upstream regions of the catchment and high basal dissipation beneath fast flowing ice streams (Figure 2b). The catchment-wide contribution to subglacial melting from basal dissipation using the 2-km inversion is 4.36×10^{10} W (SD = 5.89×10^{9} W). This contribution reduces slightly when the 5-km inversion is used (4.09×10^{10} W, SD = 5.68×10^{9} W). Due to the improved velocity misfit when the 2-km model is used, we neglect further consideration of the 5-km results.

Vertical conduction across the catchment (Figure 2c) acts as a heat sink, providing a negative contribution of 3.94×10^{10} W (SD = 1.64×10^{10} W) to the energy balance at the ice base. There are a number of isolated regions where vertical conduction acts as a heat source. However, the contributions are very small. These most likely result from the advection of warmer ice from upstream, and these regions tend to be located at the upstream extent of areas of basal frictional dissipation, at the onset of basal sliding (compare Figures 2b and 2c).

Combining the different melt rate components we see that the largest melt rates (>0.1 m $year^{-1}$) are found beneath Fisher, Mellor and Lambert glaciers (Figure 3), reaching a peak of 0.7 m $year^{-1}$ near the grounding line. The total catchment-wide subglacial melt rate is 7.03 Gt $year^{-1}$ (SD = 1.94 Gt $year^{-1}$). Integrated across the catchment, basal friction dissipation provides about 40% less energy for melting than GHF. However, this percentage varies significantly across the catchment. Heat produced from basal dissipation dominates the energy balance in the fast-flowing ice streams, where it is at least an order of magnitude greater than GHF (Figure 2). Whereas, in regions of slow flowing ice ($|u| < 10$ m $year^{-1}$) GHF is the dominant source of heat and melt rates are much smaller, 10^{-2}–10^{-3} m $year^{-1}$ (Figure 3 and Figure S11 in Supporting Information S1).

This total melt rate is substantially more (48%) than the earlier estimate from Van Liefferinge and Pattyn (2013) (Table S5 in Supporting Information S1). The largest differences arise beneath ice streams, where the high levels of melting generated by basal frictional dissipation are not well resolved by Van Liefferinge and Pattyn (2013) (Figure 3d and Figure S11b in Supporting Information S1). Our result (area-average: 5.9 mm $year^{-1}$) is also substantially higher than the melt rate from Pittard et al. (2016) (area-average: 1.3 mm $year^{-1}$). Within the Lambert Glacier and American Highlands regions of the AmISC, our melt rate (3.1 Gt $year^{-1}$) is significantly greater than that suggested by Kang et al. (2022) (0.87 Gt $year^{-1}$ using Li GHF). Our estimate produces melting throughout this region, whereas Kang et al. (2022) predict a frozen bed across much of the inland area (Figure 3c and Figure S11c in Supporting Information S1).

4.2. Subglacial Lakes

Newly discovered subglacial lakes detected from surface elevation change are shown in Figure 4. A chain of lakes is found beneath Lambert Glacier, with one of these lakes contained within the outline of a previously detected lake (Smith et al., 2009). Solitary lakes are found in the upstream parts of Mellor and Fisher glaciers, with two further solitary lakes found within regions of slow flowing ice.

21699011, 2024, 4, Downloaded from https://agupubs.onlinelibrary.wiley.com/doi/10.1029/2023JF007421 by University Of Waterloo Dana Po, Wiley Online Library on [09/08/2024]. See the Terms and Conditions (https://onlinelibrary.wiley.com/terms-and-conditions) on Wiley Online Library for rules of use; OA articles are governed by the applicable Creative Commons License

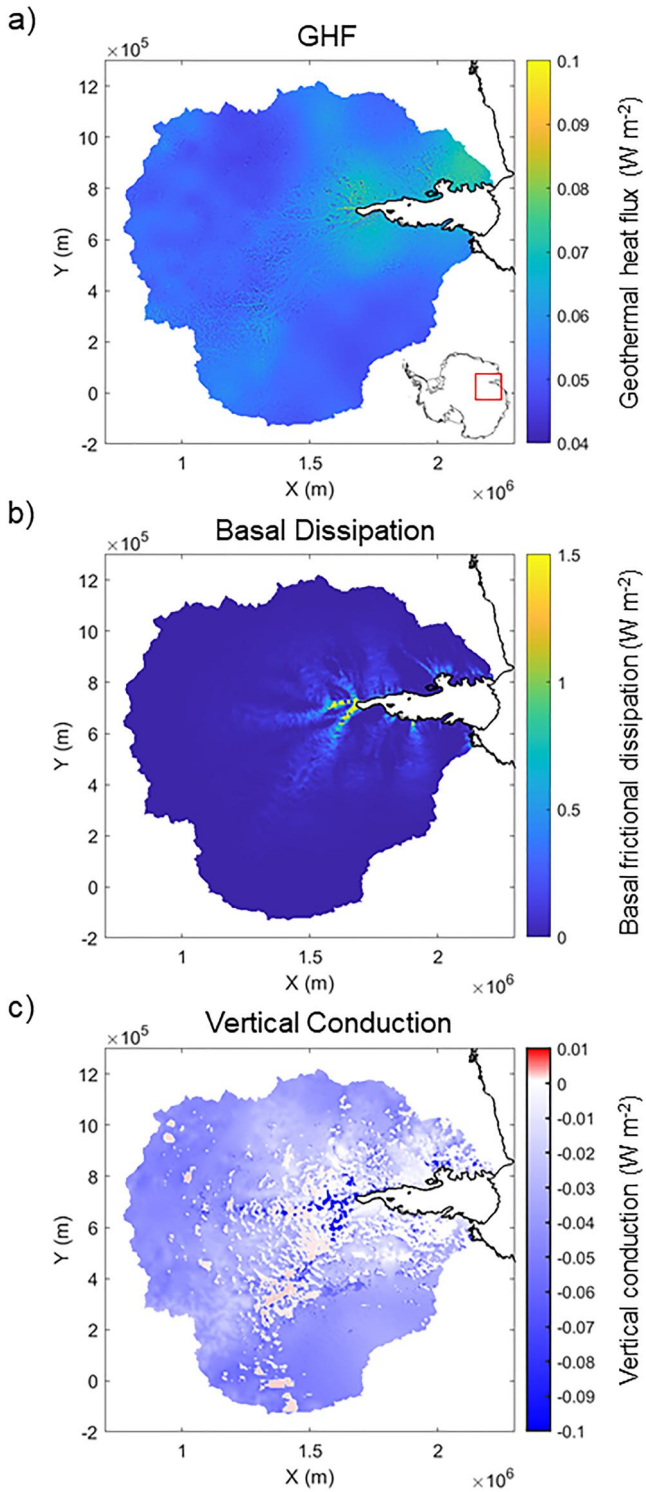


Figure 2. Subglacial melt rate components. (a) Geothermal heat flux (GHF); average of Martos and Shen GHF. (b) Basal frictional dissipation; calculated using 2-km ice-flow model inversion. (c) Vertical conduction; calculated from englacial temperature gradient, using result from Van Liefferinge and Pattyn (2013). In all panels the grounding line is in black (Depoorter et al., 2013).

4.3. Ice-Shelf Basal Melt Rates

Basal mass balance of AmIS has a distinctive pattern of melting in the upstream portion of the ice shelf (exceeding 50 m year^{-1} within 10 km of the grounding line), coincident with a deep ice shelf, and low magnitude freeze-on in the downstream portions of the shelf (Figure 4 and Figure S12 in Supporting Information S1), as reported previously (Adusumilli et al., 2020; Fricker et al., 2001; Wen et al., 2010). We observe a total basal melt rate of 12.5 Gt year $^{-1}$ (±2.4 Gt year^{-1}), which is less than previous estimates (45.6 ± 40 Gt year^{-1}: Adusumilli et al. (2020), 35.5 ± 23 Gt year^{-1}: Rignot et al. (2013)), but falls within the large uncertainty bounds of previous studies.

4.4. Meltwater Routing

Using the subglacial meltwater routing approximation, all active subglacial lakes are found on subglacial routing pathways. The chain of lakes beneath Lambert Glacier are located along a single connected pathway with maximum accumulated flux of 70 m^3 s^{-1} (Figure 5a). A second high-flux pathway is found beneath Mellor Glacier (≈60 m^3 s^{-1}). All other pathways in the catchment transport considerably less meltwater (<30 m^3 s^{-1}).

The routing method allows a straightforward assessment of the contribution to the subglacial hydrology from each of the subglacial melt rate components. The proportion of subglacial flux from meltwater produced by basal dissipation increases toward the grounding line (Figure 5b and Figure S13 in Supporting Information S1), in places reaching a maximum of 70%. Further upstream, in slower-flowing regions, the meltwater flux predominantly results from GHF (Figure S13 in Supporting Information S1). Flux across the grounding line from all subglacial pathways is higher for the Martos GHF, by 6 - 20%, compared to the Shen GHF (Figure 5c). Further upstream there are both positive and negative differences, which in some locations are up to 30% (Figure 5c and Figure S13 in Supporting Information S1).

4.5. Simulations Using GlaDS

The subglacial hydrology model (GlaDS) produces a network of channels similar to the routing approximation in the downstream portions of the catchment (Figure 6). However, using a more physically realistic model allows us to make the distinction between the channelized and distributed components of the subglacial drainage system (Figures S14 and S15 in Supporting Information S1).

When the high channel conductivity parameter is used, maximum channelized subglacial discharge at the grounding line is 70 m^3 s^{-1} (Figure 6a) with approximately 10 m^3 s^{-1} of additional discharge from the distributed system (Figure S14 in Supporting Information S1). This combined discharge is greater than the routing solution, partly as a result of slightly different catchments, but also because additional melting is generated by frictional dissipation of water flowing in the distributed system and channels (Dow, Karlsson, & Werder, 2018). When the channel conductivity parameter is reduced there is a decrease in the upstream extent of the channelized network and a decrease in channelized discharge of approximately 50% (Figure 5b). To compensate for the decrease in meltwater flux through channels there is more than a doubling of the flux within the distributed sheet (Figure S15 in Supporting Information S1).

21699011, 2024, 4, Downloaded from https://agupubs.onlinelibrary.wiley.com/doi/10.1029/2023JF007421 by University Of Waterloo Dana Po, Wiley Online Library on [09/08/2024]. See the Terms and Conditions (https://onlinelibrary.wiley.com/terms-and-conditions) on Wiley Online Library for rules of use; OA articles are governed by the applicable Creative Commons License

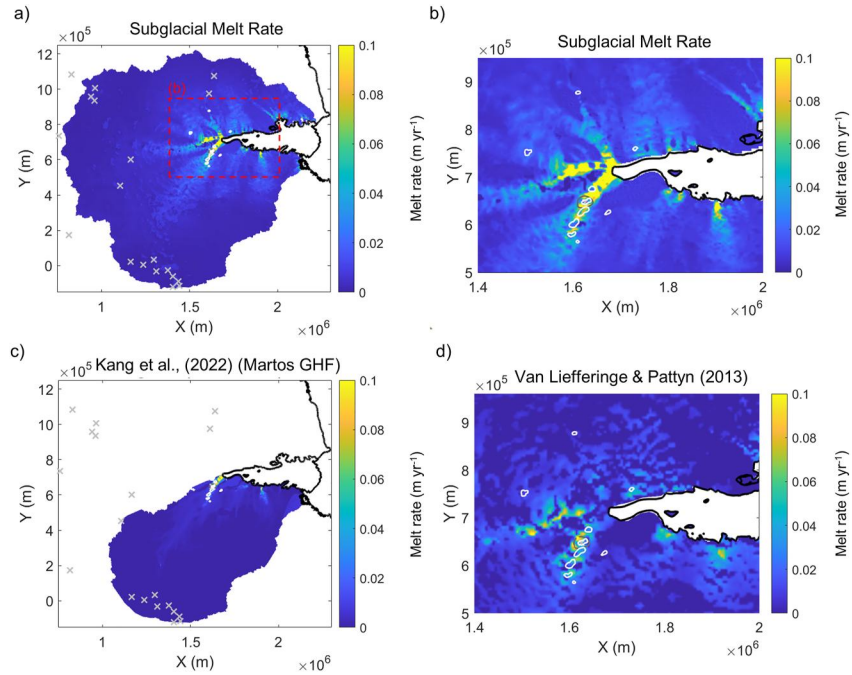


Figure 3. Subglacial melt rate: (a) Full Amery Ice Shelf catchment, with extent of panels (b) and (d) shown by red dashed rectangle. (b) Zoom-in of high melt rates beneath ice streams. (c) Subglacial melt rate within the Lambert Glacier and American Highlands regions of the AmISC from Kang et al. (2022). (d) Subglacial melt rate from Van Liefferinge and Pattyn (2013). The grounding line is shown in black (Depoorter et al., 2013). White outlines show active subglacial lakes detected by satellite altimetry. Gray crosses show subglacial lakes from inventory of Wright and Siegert (2012).

In addition to subglacial water flux, GlaDS also simulates subglacial water thickness and pressure. A distributed sheet of 1 - 10 mm thickness is present in the upstream catchment (Figure S14 in Supporting Information S1). Areas of deep subglacial water coincide with detected active subglacial lakes when high channel conductivity is used (Figure 7a and Figure S17 in Supporting Information S1). However, with low channel conductivity, additional areas of deep subglacial water are predicted, particularly along Mellor Glacier (Figure 7b). Furthermore, areas of low and negative effective pressure coincide with active subglacial lakes outlines, but are more extensive and exceed the boundaries of the subglacial lakes when low channel conductivity is used (Figure S17 in Supporting Information S1).

Although the two main subglacial discharge channels ($\geq$50 m^3 s^{-1}) are found at the southernmost section of the grounding line, there are a number of smaller channels discharging meltwater along both the East and West

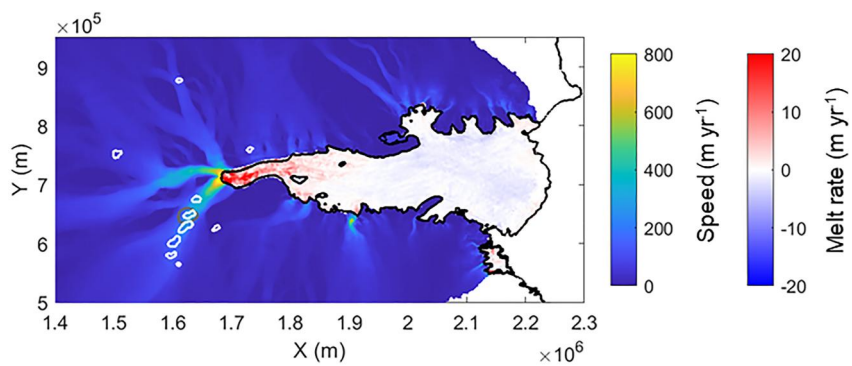


Figure 4. Subglacial lakes and ice-shelf basal melting (blue to red colorbar) detected from satellite radar altimetry. Surface velocity displayed on grounded ice (blue to yellow colorbar) (Rignot et al., 2017). Black line denotes grounding line. White outlines denote subglacial lakes detected as part of this study. Gray outline denotes previously detected subglacial lake (Smith et al., 2009).

21699011, 2024, 4, Downloaded from https://agupubs.onlinelibrary.wiley.com/doi/10.1029/2023JF007421 by University Of Waterloo Dana Po, Wiley Online Library on [09/08/2024]. See the Terms and Conditions (https://onlinelibrary.wiley.com/terms-and-conditions) on Wiley Online Library for rules of use; OA articles are governed by the applicable Creative Commons License

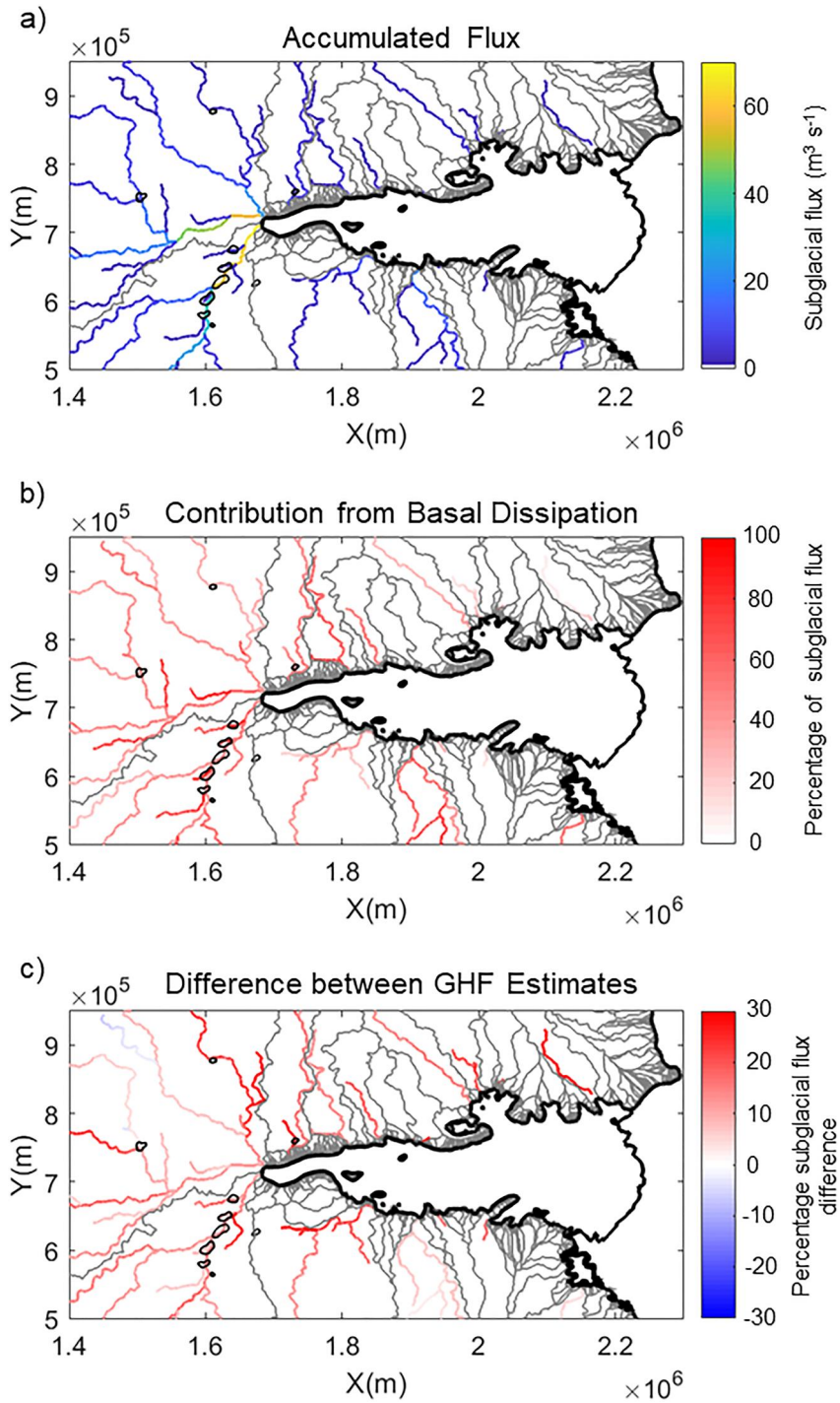


Figure 5. Subglacial routing: (a) Total accumulated meltwater flux. (b) Component of subglacial flux from meltwater produced by frictional basal dissipation (normalized by total flux (a)). (c) Difference in subglacial flux between melt rates using Martos and Shen geothermal heat flux (GHF) (normalized by total flux). Thin black outlines denote active subglacial lakes and gray outlines indicate subglacial catchments.

margins of Amery Ice Shelf (Figures 6 and 8, Figure S18 in Supporting Information S1). Three channels discharging ≥ 5 m^3 s^{-1} are found along the eastern margin, with additional channels discharging < 5 m^3 s^{-1} along both margins (Figure 8 and Figure S18 in Supporting Information S1). A cluster of four channels discharge into the embayment at the outflow of Charybdis Glacier (Figure S18 in Supporting Information S1). Comparing the

21699011, 2024, 4, Downloaded from https://agupubs.onlinelibrary.wiley.com/doi/10.1029/2023JF007421 by University Of Waterloo Dana Por, Wiley Online Library on [09/08/2024]. See the Terms and Conditions (https://onlinelibrary.wiley.com/terms-and-conditions) on Wiley Online Library for rules of use; OA articles are governed by the applicable Creative Commons License

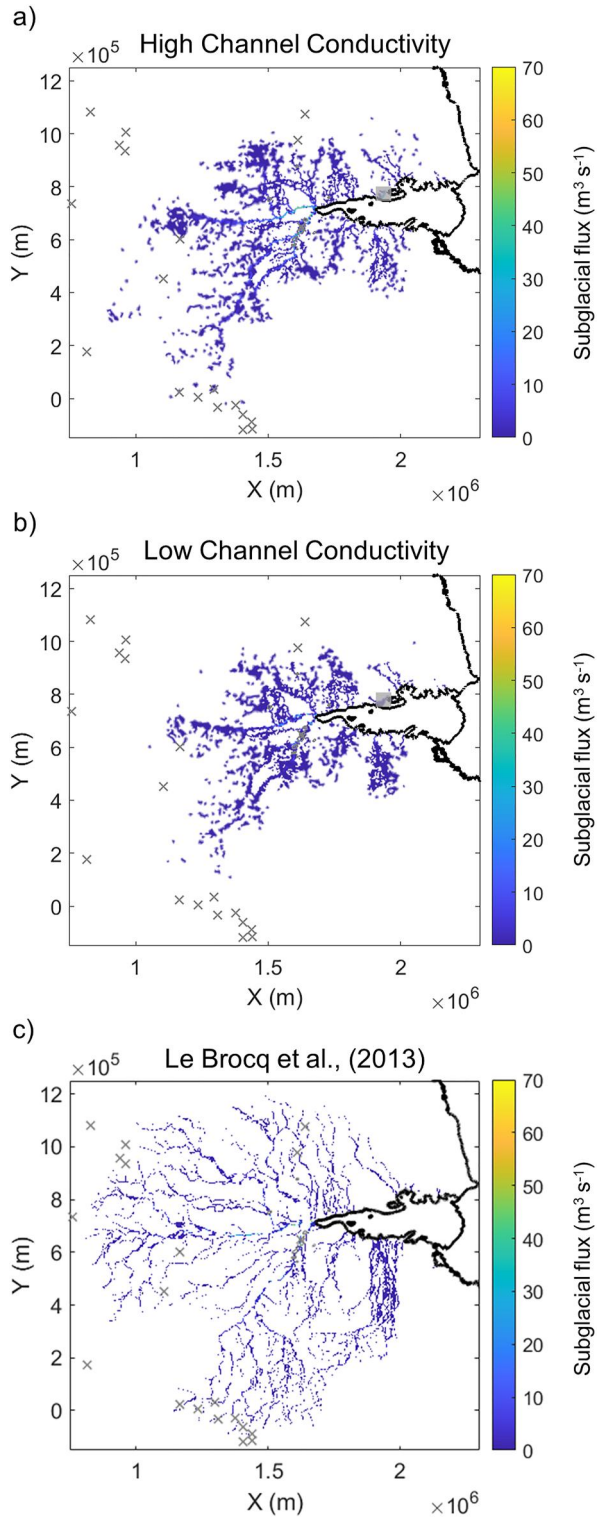


Figure 6. Channelized subglacial flux simulated by GlaDS, using high (a) and low (b) channel conductivity. (c) Subglacial flux along drainage pathways from Le Brocq et al. (2013). In all panels the grounding line is shown in black (Depoorter et al., 2013), gray outlines show active subglacial lakes detected by satellite altimetry, and gray crosses show subglacial lakes from inventory of Wright and Siegert (2012).

location of subglacial discharge channels with the observed ice-shelf basal melting, we see that along the eastern margin of the ice shelf, areas of isolated ice-shelf melting of 10 - 15 m yr^{-1} coincide with the larger subglacial discharge channels. In the case of high channel conductivity, this channelized discharge is ≥ 5 m^3 s^{-1} (Figures 8a, 8c, and 8d). However, the flux from two of the three channels is substantially reduced (< 2 m^3 s^{-1}) in the case of low channel conductivity (Figures 8b, 8e, and 8f).

5. Discussion

The main inputs for the subglacial hydrology model are the ice-surface topography, bedrock topography and subglacial melt rate. In the downstream portion of the subglacial drainage network the location and connectivity of channels in both the GlaDs simulation and routing approximation differ slightly from the drainage pathways calculated previously (Le Brocq et al., 2013) (Figure 6c and Figure S16 in Supporting Information S1). This is because we have used the latest ice-sheet bed and surface topography (Morlighem et al., 2020), while Le Brocq et al. (2013) used the earlier Bedmap2 (Fretwell et al., 2013) data set. In some places channels are missing in GlaDS, suggesting that drainage along these pathways is either absent or occurs in the distributed sheet rather than a channel. Furthermore, the flux within some channels is up to twice that previously calculated by Le Brocq et al. (2013) (Figure 6 and Figure S16 in Supporting Information S1), who used the subglacial melt rate from Pattyn (2010). We have produced a new subglacial melt rate using a higher-order ice-flow model and two estimates of GHF.

5.1. Subglacial Melt Rate

Within the AmISC the total subglacial melt rate is 7.03 Gt yr^{-1} (SD = 1.94 Gt yr^{-1}). This provides approximately 8% additional mass loss from the catchment in addition to grounding-line discharge (Rignot et al., 2013), with mass ultimately lost via ice-shelf basal melting and iceberg calving.

Integrated over the whole catchment, basal dissipation contributes approximately 40% less than GHF to the total energy balance. However, beneath fast-flowing ice streams, the contribution to subglacial melting from basal dissipation is an order of magnitude greater than GHF. This leads to a significant increase in subglacial flux as channels approach the grounding line, with up to 70% of the meltwater produced by basal dissipation.

5.1.1. Uncertainty in Melt Rate Components

The largest uncertainty in catchment-wide subglacial melt rate corresponds to the vertical conduction component (SD = 1.64×10^{10} W). This is partly because we have taken a conservative approach to represent this uncertainty, capturing the uncertainty in englacial temperature from Van Liefferinge and Pattyn (2013), and also the inconsistency between the GHF used by Van Liefferinge and Pattyn (2013), and that from Martos et al. (2017) and Shen et al. (2020), as used here.

Variations in estimates of GHF derived from magnetic and seismic surveys (Martos et al., 2017 and Shen et al., 2020 respectively), result in the GHF component of subglacial melt rate having the second largest uncertainty, (SD = 1.06×10^{10} W). Meanwhile, the basal dissipation component has the smallest uncertainty (SD = 8.08×10^{9} W). Improved observations of ice velocity, particularly in slow-flowing regions (Mouginot et al., 2019), and

21699011, 2024, 4, Downloaded from https://agupubs.onlinelibrary.wiley.com/doi/10.1029/2023JF007421 by University Of Waterloo Dana Po, Wiley Online Library on [09/08/2024]. See the Terms and Conditions (https://onlinelibrary.wiley.com/terms-and-conditions) on Wiley Online Library for rules of use; OA articles are governed by the applicable Creative Commons License

21699011, 2024, 4, Downloaded from https://agupubs.onlinelibrary.wiley.com/doi/10.1029/2023JF007421 by University Of Waterloo Dana Po, Wiley Online Library on [09/08/2024]. See the Terms and Conditions (https://onlinelibrary.wiley.com/terms-and-conditions) on Wiley Online Library for rules of use; OA articles are governed by the applicable Creative Commons License

analysis of posterior uncertainty in ice-flow model inversions could be used to further clarify the uncertainty associated with basal dissipation.

Reducing the grid resolution (from 2-km to 5-km) of the ice-sheet model leads to a small reduction (7%) in the basal dissipation contribution to melting, with the largest differences occurring where there are sharp gradients in ice-flow speed (e.g., ice-stream margins). These results suggest that a higher-order ice-flow model with 5-km resolution may be suitable, and computationally viable, for determining Antarctic-wide basal dissipation. Furthermore, the large and spatially complex contribution to subglacial melting from basal dissipation highlights that a uniform subglacial melt rate (Dow, Karlsson, & Werder, 2018; Wei et al., 2020) is an inappropriate input to a subglacial hydrology model.

5.1.2. Comparison With Previous Subglacial Melt Rate Products

The total subglacial melt rate calculated here is considerably higher than previous estimates. It is 48% greater than the value from Van Liefferinge and Pattyn (2013). This is largely because we are able to resolve high basal frictional dissipation beneath the fast-flowing ice streams (Figure 3) using the increased capability of the higher-order ice flow model.

Our subglacial melt rate is 3-4.5 times larger than the melt rates calculated using thermo-mechanical models (for the full catchment; Pittard et al., 2016 and part of catchment; Kang et al., 2022). These previous results indicate frozen bed conditions in the upstream parts of the catchment, where we simulate low-level melting, with heating from both basal dissipation and GHF. Kang et al. (2022) required the highest estimate of GHF (Li et al., 2021) to produce any melting in these upstream regions where subglacial lakes (assumed to be inactive) have been detected from ice-penetrating radar (see Figures 1, 3, and 6 for lake locations (Wright & Siegert, 2012) and Kang et al. (2022); Figure 9). The presence of these lakes suggests subglacial melting in these upstream regions. These studies assume a steady-state englacial temperature in equilibrium with modern climate and must solve both the ice-flow and thermal problem consistently, which can potentially lead to a larger misfit with velocity observations and reduce basal dissipation. Furthermore, Kang et al. (2022) effectively smoothed their basal friction parameter, to account for the transition between a frozen and thawed bed, which potentially further reduced the simulated contribution from basal dissipation. However, the thermo-mechanical approach does provide consistency between GHF and englacial temperature. Our approach has calculated these components separately and we have accounted for the uncertainty associated with this by using a conservative estimate of uncertainty in the vertical temperate gradient, which provides the largest uncertainty in this assessment.

5.2. Subglacial Hydrology

The discharge of freshwater from subglacial melting is approximately 36% of the total freshwater released into the AmIS cavity in addition to that produced by ice-shelf basal melting. The magnitude and localised distribution of this freshwater discharge at depth is important for ocean circulation within the ice-shelf cavity, with implications for ice-shelf basal melt, freeze-on (Galton-Fenzi et al., 2012; Gwyther et al., 2023; Jenkins, 2011) and marine biological productivity (Death et al., 2014; Herraiz-Borreguero et al., 2016; St-Laurent et al., 2017).

We assess the impact of different subglacial melt rate components on subglacial hydrology using a routing approximation. We find that in the slow-flowing upstream areas of the catchment, where GHF is the main source of melting, the uncertainty in subglacial meltwater flux can be up to 30% due to the uncertainty in GHF estimates (Figure 5). Recent advances in the detection and monitoring of active subglacial lakes using satellite altimetry (Malczyk et al., 2020; Smith et al., 2017) signal the potential to combine the observed filling rates of lakes and subglacial hydrology modelling in these areas to further constrain GHF (Malczyk et al., 2023).

GlaDS simulates both the channelized and distributed components of subglacial hydrology, and is therefore more physically realistic than a routing approximation or models that do not make this distinction (Le Brocq et al., 2009; Smith et al., 2017). This is particularly clear in Figure 6, where channels are absent in the upper parts of the catchment in GlaDS and subglacial drainage is confined to the distributed sheet.

5.2.1. Comparing Subglacial Hydrology With Observations

The network of subglacial channels does not extend upstream as far as the subglacial lakes detected from ice-penetrating radar (Wright & Siegert, 2012), when high channel conductivity is used. In the case of low

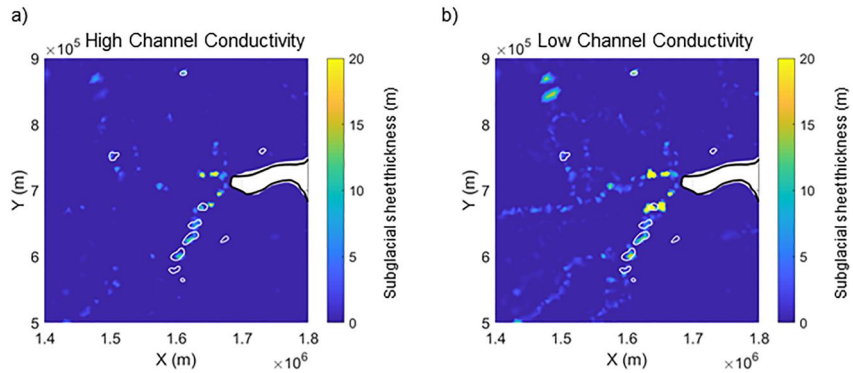


Figure 7. Subglacial water thickness simulated by GlaDS, using high (a) and low (b) channel conductivity. White outlines denote subglacial lakes detected from satellite altimetry.

channel conductivity, a few lakes coincide with the upstream extent of some channels. The fact that this set of subglacial lakes is largely disconnected from subglacial channels supports the idea that these lakes are non-active, and there is a clear distinction between these lakes and the active lakes found in the downstream parts of the subglacial network.

Comparing GlaDS results with remote-sensing observations suggests a high channel conductivity parameter (1×10^{-2} $m^{3/2}$ $kg^{-1/2}$) is the most appropriate choice for the AmISC. First, for high channel conductivity, areas of deep subglacial water and low effective pressure match with the locations of subglacial lakes (Figure 7 and Figure S16 in Supporting Information S1). In contrast, low conductivity leads to more extensive areas of low effective pressure that extend beyond the bounds of lakes and additional areas of deep water that have not been identified as subglacial lakes. Second, channelized discharge along the eastern margin of the ice shelf is coincident with isolated regions of ice-shelf basal melting (Figure 8). These subglacial channels have up to 60% less flux when the lower channel conductivity parameter is used (1×10^{-3} $m^{3/2}$ $kg^{-1/2}$) (Figure 8), and in places the discharge decreases to less than 2 m^3 s^{-1}, reducing the likelihood of enhanced melting.

The isolated areas of ice-shelf melting likely result from a buoyant plume triggered by freshwater discharge that entrains relatively warm ambient ocean water at depth (Dallaston et al., 2015; Jenkins, 2011). It is unlikely that discharge from the distributed subglacial sheet could trigger this melting, because it is an order of magnitude smaller than channelized discharge, and approximately evenly distributed along the grounding line (Figure S18 in

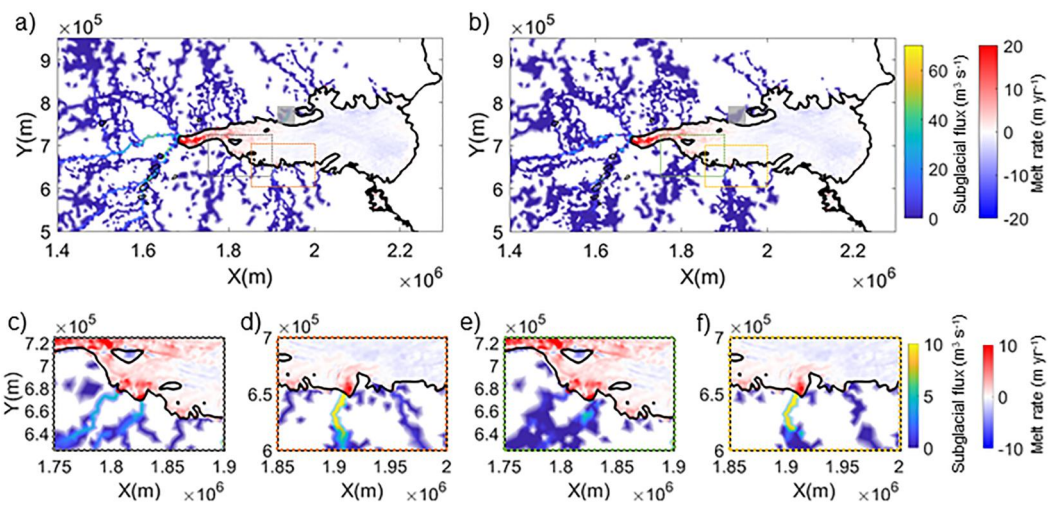


Figure 8. Channelized subglacial flux (GlaDS) and ice-shelf basal melting. (a) High channel conductivity. (b) Low channel conductivity. Panels (c)–(f) show zoom-in view around subglacial discharge and isolated ice-shelf basal melting. Extent of (c)–(f) is shown in (a) and (b).

21699011, 2024, 4, Downloaded from https://agupubs.onlinelibrary.wiley.com/doi/10.1029/2023JF007421 by University Of Waterloo Dana Po, Wiley Online Library on [09/08/2024]. See the Terms and Conditions (https://onlinelibrary.wiley.com/terms-and-conditions) on Wiley Online Library for rules of use; OA articles are governed by the applicable Creative Commons License

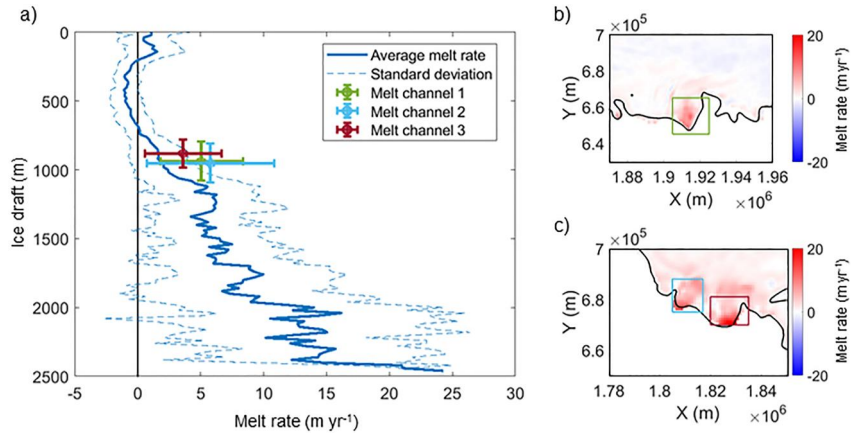


Figure 9. (a) Ice-shelf wide average melt rate versus ice draft (depth below sea level). Bold blue line represents mean melt rate at 20 m depth intervals. Dashed blue line represents standard deviation of melt rate. Points and error bars represent data from each of the subglacial discharge locations. (b) Ice shelf area adjacent to melt channel 1 (green rectangle). (c) Ice shelf area adjacent to melt channel 2 (blue rectangle) and 3 (red rectangle).

Supporting Information S1). Furthermore, to clarify that this focused melting is not the result of pressure dependent melting where a thick glacier enters the ice shelf, we plot the depth-averaged melt rate across the whole ice shelf in Figure 9. We see that the melt rate at the subglacial discharge channel locations is one standard deviation, or more, greater than the average melt rate at the same depth elsewhere on the ice shelf (Figure 9). The magnitude of ice-shelf basal melting expected from varying channelized discharge could be further clarified with a dedicated ocean modelling study.

5.2.2. Insights From the Validated Model

This optimum channel conductivity parameter (1×10^{-2} $m^{3/2}$ $kg^{-1/2}$) is less than the value used previously (5×10^{-2} $m^{3/2}$ $kg^{-1/2}$: Aurora Subglacial Basin (Dow et al., 2020), Recovery Glacier (Dow, Karlsson, & Werder, 2018), and Gornergletscher (Werder et al., 2013)). Our initial simulations using this value led to unstable channel growth. However, the subglacial melt rates and fluxes here are greater than in previous studies ($Q < 25$ m^3 s^{-1}; Dow et al., 2020, $Q < 11$ m^3 s^{-1}; Dow, Karlsson, & Werder, 2018), suggesting that despite reduced channel conductivity, which would act to suppress channel formation and growth (Dow et al., 2016), high-flux channels still occur.

Despite being a more physically realistic representation of the subglacial hydrology than a routing approximation, GlaDS does not include specific physics to simulate the filling and draining of subglacial lakes. However, the coincidence of simulated deep subglacial water and detected active lakes suggests that the model can simulate some of the associated processes. Future studies could use deep subglacial water predicted by subglacial hydrology models to aid the detection of subglacial lakes.

Visually we observe that effective pressure (simulated by GlaDS) and basal friction parameter (β^2: inferred by ice-flow model) have a similar spatial distribution, with areas of low effective pressure coinciding with low β^2 (Figure S19 in Supporting Information S1). Although this relationship is statistically significant ($p < 0.01$), the correlation between the two parameters is relatively low (Spearman correlation = 0.37). However, it does hint at the expected influence of subglacial hydrology on ice-sheet flow (Alley, 1996; Hewitt, 2013; Joughin et al., 2003) and could be investigated further using a coupled ice-flow and subglacial-hydrology model (e.g., Hoffman & Price, 2014).

Previous use of GlaDS in the Aurora Subglacial Basin has used radar specularity to constrain the sheet conductivity parameter (Dow et al., 2020), while here we have constrained the channel conductivity parameter using observations of subglacial lakes and ice-shelf basal melting. Future work could combine these approaches to further clarify subglacial conditions.

21699011, 2024, 4, Downloaded from https://agupubs.onlinelibrary.wiley.com/doi/10.1029/2023JF007421 by University Of Waterloo Dana Po, Wiley Online Library on [09/08/2024]. See the Terms and Conditions (https://onlinelibrary.wiley.com/terms-and-conditions) on Wiley Online Library for rules of use; OA articles are governed by the applicable Creative Commons License

21699011, 2024, 4, Downloaded from https://agupubs.onlinelibrary.wiley.com/doi/10.1029/2023JF007421 by University Of Waterloo Dana Po, Wiley Online Library on [09/08/2024]. See the Terms and Conditions (https://onlinelibrary.wiley.com/terms-and-conditions) on Wiley Online Library for rules of use; OA articles are governed by the applicable Creative Commons License

5.2.3. Influence of Subglacial Hydrology on Dynamics and Stability of AmISC

At present the AmISC is relatively stable, with little change in the ice thickness (Smith et al., 2020), ice speed (King et al., 2007) and periodic calving of large tabular icebergs (Fricker et al., 2002). Increased ice discharge could result from increased subglacial melting and lubrication at the ice-bed interface. One possible source of meltwater to increase basal lubrication may be surface meltwater drainage to the bed, as is the case along the margins of the Greenland Ice Sheet (Karlsson et al., 2021). Although climate modeling suggests this would only be possible with 4°C of warming (Gilbert & Kittel, 2021), surface meltwater has been observed in the vicinity of the AmIS grounding line since at least the 1970s (Spergel et al., 2021). Other changes in catchment dynamics could result from decreases in ice-shelf buttressing through processes such as increased ice-shelf basal melting (Reese et al., 2018), basal-channel incision (Dow, Lee, et al., 2018; Rignot & Steffen, 2008), hydrofracture (Lai et al., 2020; Scambos et al., 2009) or increased calving (Joughin et al., 2021). This could accelerate ice-stream flow and in turn increase the basal frictional dissipation contribution to subglacial melting. However, Dawson et al. (2022) have shown that this catchment is relatively stable to increases in the spatial extent of thawed and sliding bed conditions, with an increase in ice-sheet mass balance of <5 Gt year^{-1} when the extent of the thawed region is increased to areas currently up to 8°C below the pressure melting point.

Our observations indicate a chain of active subglacial lakes beneath Lambert Glacier. The filling and draining cycle of these lakes likely affects the subglacial water pressure and may influence the temporal variability of ice dynamics for this ice stream as has been observed previously for Byrd Glacier (Stearns et al., 2008) and many Greenlandic glaciers (e.g., Davison et al., 2019; Livingstone et al., 2019). To investigate this further would require observations of ice velocity and surface elevation change at high spatial and temporal resolution in this area to determine the influence of active lakes on ice dynamics.

Importantly, our results demonstrate the influence of concentrated subglacial discharge on the distribution of ice-shelf basal melt rates, highlighting that the location and magnitude of subglacial discharge should be considered when simulating ocean melting of ice shelves (e.g., Goldberg et al., 2023; Gwyther et al., 2023) and that temporal variations in subglacial hydrology, due to subglacial lake activity or channel rerouting, could impact ice-shelf basal melting.

6. Conclusion

Using the subglacial hydrology model GlaDS we have simulated the subglacial hydrology within the AmISC and validated the results using observations of active subglacial lakes and ice-shelf basal melting from high-resolution satellite radar altimetry. We find that the subglacial hydrology system consists of drainage through a thin distributed sheet in the upstream sections of the catchment, which feeds into a network of channels downstream. These channels link areas of deep subglacial water at high pressure, that are coincident with the locations of active subglacial lakes. The main subglacial drainage channels are found beneath the fast-flowing ice streams, with channelized discharge at the grounding line triggering enhanced ice-shelf basal melting.

The main input to the subglacial hydrology model is subglacial melt rate, calculated using an ice-flow model and two estimates of GHF. The total basal melt rate within the AmISC is 7.03 Gt year^{-1} (SD = 1.94 Gt year^{-1}), with the largest uncertainties associated with vertical conduction and GHF. The total subglacial melt rate is substantially more than previous estimates. This is partly due to improved data sets and simulation of basal dissipation using a higher-order ice-flow model, which shows subglacial melting in the upstream slow-flowing regions of the catchment, where previous studies suggest the ice-sheet bed is frozen. Across the catchment, basal friction dissipation provides about 40% less energy for melting than GHF, but beneath the fast-flowing ice streams the contribution from basal dissipation is an order of magnitude larger than GHF. GHF uncertainty is most critical in areas of slow-flowing ice, where it is the main heat source for melting, leading to higher uncertainties in the subglacial flux within the upstream parts of the catchment.

We have detected a chain of active subglacial lakes beneath Lambert Glacier and several other solitary subglacial lakes within the AmISC using interferometric-swath radar altimetry. We also generated a new map of ice-shelf basal melting, observing high melt rates in the upstream portion of the ice shelf and freeze-on downstream. Using these observations, we validated the channel conductivity parameter within the subglacial hydrology model GlaDS. The ability to validate the subglacial model provides crucial insight into this

largely unobservable subglacial environment, such as the spatial extent of channelized and distributed drainage networks, the flux within subglacial channels, the subglacial water thickness and potentially locations of subglacial lakes, and the magnitude of subglacial water pressure, which plays an important role in the dynamics of the overlying ice. We additionally find that outlets of subglacial channels with discharge >5 $m^3 s^{-1}$ coincide with isolated regions of increased ice-shelf basal melting that are not sufficiently explainable by ice thickness alone, suggesting focused discharge of fresh subglacial meltwater triggers enhanced melting.

The discharge of subglacial meltwater provides approximately 36% of the freshwater released into the ice-shelf cavity and this release is largely concentrated where subglacial channels intersect the grounding line. This concentrated discharge should be considered in investigations of ocean circulation within the ice-shelf cavity, including numerical simulations, in-situ and remote-sensing observations, in order to accurately capture the impact on ice-shelf basal melting, and the wider influence on sea ice and biological productivity.

Data Availability Statement

The model output generated during this project, including subglacial melt rates and hydrology model results, along with ice-shelf basal melt rates and subglacial lake outlines are available here: https://doi.org/10.6084/m9.figshare.16447251.v1.

The original GHF products from Martos et al. (2017) and Shen et al. (2020) are available here:

Martos GHF: https://doi.pangaea.de/10.1594/PANGAEA.882503.
Shen GHF: https://sites.google.com/view/weisen/research-products?authuser=0.

Acknowledgments
M. Wearing, D. Goldberg, N. Gourmelen and A. Hogg acknowledge funding from the European Space Agency (ESA) via the 4DAntarctica project grant number: 4000128611/19/I-DT. N. Gourmelen and L. Jakob acknowledges funding from the ESA Polar + Ice Shelf project ref: 4000132186/20/I-EF. C. Dow acknowledges support from the Natural Sciences and Engineering Research Council of Canada (NSERC RGPIN-03761-2017) and the Canada Research Chairs Program (CRC 950-231237). The authors gratefully acknowledge the ESA for the acquisition of CryoSat-2 data.

References

Adusumilli, S., Fricker, H. A., Medley, B., Padman, L., & Siegfried, M. R. (2020). Interannual variations in meltwater input to the Southern Ocean from Antarctic ice shelves. *Nature Geoscience*, *13*(9), 616–620. https://doi.org/10.1038/s41561-020-0616-z

Alley, R. B. (1996). Towards a hydrological model for computerized ice-sheet simulations. *Hydrological Processes*, *10*(4), 649–660. https://doi.org/10.1002/(sici)1099-1085(199604)10:4⟨649::aid-hyp397⟩3.0.co;2-1

Burton-Johnson, A., Dziadek, R., & Martin, C. (2020). Review article: Geothermal heat flow in Antarctica: Current and future directions. *The Cryosphere*, *14*(11), 3843–3873. https://doi.org/10.5194/tc-14-3843-2020

Colgan, W., MacGregor, J. A., Mankoff, K. D., Haagenson, R., Rajaram, H., Martos, Y. M., et al. (2021). Topographic correction of geothermal heat flux in Greenland and Antarctica. *Journal of Geophysical Research: Earth Surface*, *126*(2), 1–26. https://doi.org/10.1029/2020jf005598

Cuffey, K. M., & Paterson, W. S. B. (2010). *The physics of glaciers* (4th ed.). Elsevier.

Dallaston, M. C., Hewitt, I. J., & Wells, A. J. (2015). Channelization of plumes beneath ice shelves. *Journal of Fluid Mechanics*, *785*, 109–134. https://doi.org/10.1017/jfm.2015.609

Davison, B. J., Sole, A. J., Livingstone, S. J., Cowton, T. R., & Nienow, P. W. (2019). The influence of hydrology on the dynamics of land-terminating sectors of the Greenland ice sheet. *Frontiers in Earth Science*, *7*, 10. https://doi.org/10.3389/feart.2019.00010

Dawson, E. J., Schroeder, D. M., Chu, W., Mantelli, E., & Seroussi, H. (2022). Ice mass loss sensitivity to the Antarctic ice sheet basal thermal state. *Nature Communications*, *13*(1), 1–19. https://doi.org/10.1038/s41467-022-32632-2

Death, R., Wadham, J. L., Monteiro, F., Le Brocq, A. M., Tranter, M., Ridgwell, A., et al. (2014). Antarctic ice sheet fertilises the Southern Ocean. *Biogeosciences*, *11*(10), 2635–2643. https://doi.org/10.5194/bg-11-2635-2014

Depoorter, M. A., Bamber, J. L., Griggs, J. A., Lenaerts, J. T. M., Ligtenberg, S. R. M., van den Broeke, M. R., & Moholdt, G. (2013). Calving fluxes and basal melt rates of Antarctic ice shelves. *Nature*, *502*(7469), 89–92. https://doi.org/10.1038/nature12567

Dow, C. F., Karlsson, N. B., & Werder, M. A. (2018). Limited impact of subglacial supercooling freeze-on for Greenland ice sheet stratigraphy. *Geophysical Research Letters*, *45*(3), 1481–1489. https://doi.org/10.1002/2017GL076251

Dow, C. F., Lee, W. S., Greenbaum, J. S., Greene, C. A., Blankenship, D. D., Poinar, K., et al. (2018). Basal channels drive active surface hydrology and transverse ice shelf fracture. *Science Advances*, *4*(6), eaao7212. https://doi.org/10.1126/sciadv.aao7212

Dow, C. F., McCormack, F. S., Young, D. A., Greenbaum, J. S., Roberts, J. L., & Blankenship, D. D. (2020). Totten glacier subglacial hydrology determined from geophysics and modeling. *Earth and Planetary Science Letters*, *531*, 115961. https://doi.org/10.1016/j.epsl.2019.115961

Dow, C. F., Werder, M. A., Nowicki, S., & Walker, R. T. (2016). Modeling Antarctic subglacial lake filling and drainage cycles. *The Cryosphere*, *10*(4), 1381–1393. https://doi.org/10.5194/tc-10-1381-2016

Flowers, G. E. (2015). Modelling water flow under glaciers and ice sheets. *Proceedings of the Royal Society A: Mathematical, Physical and Engineering Sciences*, *471*(2176), 20140907. https://doi.org/10.1098/rspa.2014.0907

Fox Maule, C., Purucker, M. E., Olsen, N., & Mosegaard, K. (2005). Heat flux anomalies in Antarctica revealed by satellite magnetic data. *Science*, *309*(5733), 464–467. https://doi.org/10.1126/science.1106888

Fretwell, P., Pritchard, H. D., Vaughan, D. G., Bamber, J. L., Barrand, N. E., Bell, R., et al. (2013). Bedmap2: Improved ice bed, surface and thickness datasets for Antarctica. *The Cryosphere*, *7*(1), 375–393. https://doi.org/10.5194/tc-7-375-2013

Fricker, H. A., Popov, S., Allison, I., & Young, N. (2001). Distribution of marine ice beneath the Amery Ice Shelf. *Geophysical Research Letters*, *28*(11), 2241–2244. https://doi.org/10.1029/2000GL012461

Fricker, H. A., Scambos, T., Bindschadler, R., & Padman, L. (2007). An active subglacial water system in West Antarctica mapped from space. *Science*, *315*(5818), 1544–1548. https://doi.org/10.1126/science.1136897

Fricker, H. A., Young, N. W., Allison, I., & Coleman, R. (2002). Iceberg calving from the Amery Ice Shelf, East Antarctica. *Annals of Glaciology*, *34*(May 2021), 241–246. https://doi.org/10.3189/172756402781817581

21699011, 2024, 4, Downloaded from https://agupubs.onlinelibrary.wiley.com/doi/10.1029/2023JF007421 by University Of Waterloo Dana Po, Wiley Online Library on [09/08/2024]. See the Terms and Conditions (https://onlinelibrary.wiley.com/terms-and-conditions) on Wiley Online Library for rules of use; OA articles are governed by the applicable Creative Commons License

Fürst, J. J., Durand, G., Gillet-Chaulet, F., Tavard, L., Rankl, M., Braun, M., & Gagliardini, O. (2016). The safety band of Antarctic ice shelves. *Nature Climate Change*, *6*(5), 479–482. https://doi.org/10.1038/nclimate2912

Galton-Fenzi, B. K., Hunter, J. R., Coleman, R., Marsland, S. J., & Warner, R. C. (2012). Modeling the basal melting and marine ice accretion of the Amery Ice Shelf. *Journal of Geophysical Research*, *117*(9), 1–19. https://doi.org/10.1029/2012JC008214

Gardner, A. S., Fahnestock, M. A., & Scambos, T. A. (2019). ITS_LIVE regional glacier and ice sheet surface velocities. https://doi.org/10.5067/6II6VW8LLWJ7

Gilbert, E., & Kittel, C. (2021). Surface melt and runoff on Antarctic ice shelves at 1.5°C, 2°C, and 4°C of future warming. *Geophysical Research Letters*, *48*(8), 1–9. https://doi.org/10.1029/2020GL091733

Goldberg, D. N. (2011). A variationally derived, depth-integrated approximation to a higher-order glaciological flow model. *Journal of Glaciology*, *57*(201), 157–170. https://doi.org/10.3189/002214311795306763

Goldberg, D. N., Gourmelen, N., Kimura, S., Millan, R., & Snow, K. (2019). How accurately should we model ice shelf melt rates? *Geophysical Research Letters*, *46*(1), 189–199. https://doi.org/10.1029/2018GL080383

Goldberg, D. N., & Sergienko, O. V. (2011). Data assimilation using a hybrid ice flow model. *The Cryosphere*, *5*(2), 315–327. https://doi.org/10.5194/tc-5-315-2011

Goldberg, D. N., Twelves, A. G., Holland, P. R., & Wearing, M. G. (2023). The non-local impacts of Antarctic subglacial runoff. *Journal of Geophysical Research: Oceans*, *128*, e2023JC019823. https://doi.org/10.1029/2023JC019823

Gourmelen, N., Escorihuela, M. J., Shepherd, A., Foresta, L., Muir, A., Garcia-Mondéjar, A., et al. (2018). CryoSat-2 swath interferometric altimetry for mapping ice elevation and elevation change. *Advances in Space Research*, *62*(6), 1226–1242. https://doi.org/10.1016/j.asr.2017.11.014

Gourmelen, N., Goldberg, D. N., Snow, K., Henley, S. F., Bingham, R. G., Kimura, S., et al. (2017). Channelized melting drives thinning under a rapidly melting Antarctic Ice Shelf. *Geophysical Research Letters*, *44*(19), 9796–9804. https://doi.org/10.1002/2017GL074929

Gwyther, D. E., Dow, C. F., Jendersie, S., Gourmelen, N., & Galton-Fenzi, B. K. (2023). Subglacial freshwater drainage increases simulated basal melt of the Totten ice shelf. *Geophysical Research Letters*, *50*(12), e2023GL103765. https://doi.org/10.1029/2023GL103765

Herraiz-Borreguero, L., Lannuzel, D., van der Merwe, P., Treverrow, A., & Pedro, J. B. (2016). Large flux of iron from the Amery Ice Shelf marine ice to Prydz Bay, East Antarctica. *Journal of Geophysical Research: Oceans*, *121*(8), 6009–6020. https://doi.org/10.1002/2016JC011687

Hewitt, I. J. (2013). Seasonal changes in ice sheet motion due to melt water lubrication. *Earth and Planetary Science Letters*, *371–372*, 16–25. https://doi.org/10.1016/j.epsl.2013.04.022

Hoffman, M., & Price, S. (2014). Feedbacks between coupled subglacial hydrology and glacier dynamics. *Journal of Geophysical Research: Earth Surface*, *119*(3), 414–436. https://doi.org/10.1002/2013JF002943

Isaac, T., Petra, N., Stadler, G., & Ghattas, O. (2015). Scalable and efficient algorithms for the propagation of uncertainty from data through inference to prediction for large-scale problems, with application to flow of the Antarctic ice sheet. *Journal of Computational Physics*, *296*, 348–368. https://doi.org/10.1016/j.jcp.2015.04.047

Jenkins, A. (2011). Convection-driven melting near the grounding lines of ice shelves and tidewater glaciers. *Journal of Physical Oceanography*, *41*(12), 2279–2294. https://doi.org/10.1175/JPO-D-11-03.1

Joughin, I., Shapero, D., Smith, B., Dutrieux, P., & Barham, M. (2021). Ice-shelf retreat drives recent Pine Island Glacier speedup. *Science Advances*, *7*(24), eabg3080. https://doi.org/10.1126/sciadv.abg3080

Joughin, I., Tulaczyk, S., Bamber, J. L., Blankenship, D., Holt, J. W., Scambos, T., & Vaughan, D. G. (2009). Basal conditions for Pine Island and Thwaites Glaciers, West Antarctica, determined using satellite and airborne data. *Journal of Glaciology*, *55*(190), 245–257. https://doi.org/10.3189/002214309788608705

Joughin, I., Tulaczyk, S., & Engelhardt, H. F. (2003). Basal melt beneath Whillans Ice Stream and Ice Streams A and C, West Antarctica. *Annals of Glaciology*, *36*(May 2021), 257–262. https://doi.org/10.3189/172756403781816130

Kang, H., Zhao, L., Wolovick, M., & Moore, J. C. (2022). Evaluation of six geothermal heat flux maps for the Antarctic Lambert–Amery glacial system. *The Cryosphere*, *16*(9), 3619–3633. https://doi.org/10.5194/tc-16-3619-2022

Karlsson, N. B., Solgaard, A. M., Mankoff, K. D., Gillet-Chaulet, F., MacGregor, J. A., Box, J. E., et al. (2021). A first constraint on basal melt-water production of the Greenland ice sheet. *Nature Communications*, *12*(1), 3461. https://doi.org/10.1038/s41467-021-23739-z

King, M. A., Coleman, R., Morgan, P. J., & Hurd, R. S. (2007). Velocity change of the Amery Ice Shelf, East Antarctica, during the period 1968–1999. *Journal of Geophysical Research*, *112*(F1), F01013. https://doi.org/10.1029/2006JF000609

Lai, C.-Y., Kingslake, J., Wearing, M. G., Chen, P.-H. C., Gentine, P., Li, H., et al. (2020). Vulnerability of Antarctica's ice shelves to meltwater-driven fracture. *Nature*, *584*(7822), 574–578. https://doi.org/10.1038/s41586-020-2627-8

Le Brocq, A. M., Payne, A. J., Siegert, M. J., & Alley, R. B. (2009). A subglacial water-flow model for West Antarctica. *Journal of Glaciology*, *55*(193), 879–888. https://doi.org/10.3189/002214309790152564

Le Brocq, A. M., Ross, N., Griggs, J. A., Bingham, R. G., Corr, H. F., Ferraccioli, F., et al. (2013). Evidence from ice shelves for channelized meltwater flow beneath the Antarctic ice sheet. *Nature Geoscience*, *6*(11), 945–948. https://doi.org/10.1038/ngeo1977

Li, L., Tang, X., Guo, J., Cui, X., Xiao, E., Latif, K., et al. (2021). Inversion of geothermal heat flux under the ice sheet of Princess Elizabeth Land, East Antarctica. *Remote Sensing*, *13*(14), 2760. https://doi.org/10.3390/rs13142760

Livingstone, S. J., Li, Y., Rutishauser, A., Sanderson, R. J., Winter, K., Mikucki, J. A., et al. (2022). Subglacial lakes and their changing role in a warming climate. *Nature Reviews Earth & Environment*, *3*(2), 106–124. https://doi.org/10.1038/s43017-021-00246-9

Livingstone, S. J., Sole, A. J., Storrar, R. D., Harrison, D., Ross, N., & Bowling, J. (2019). Brief communication: Subglacial lake drainage beneath Isunguata Sermia, West Greenland: Geomorphic and ice dynamic effects. *The Cryosphere*, *13*(10), 2789–2796. https://doi.org/10.5194/tc-13-2789-2019

Malczyk, G., Gourmelen, N., Goldberg, D., Wuite, J., & Nagler, T. (2020). Repeat subglacial lake drainage and filling beneath Thwaites glacier. *Geophysical Research Letters*, *47*(23), e2020GL089658. https://doi.org/10.1029/2020GL089658

Malczyk, G., Gourmelen, N., Werder, M., Wearing, M., & Goldberg, D. (2023). Constraints on subglacial melt fluxes from observations of active subglacial lake recharge. *Journal of Glaciology*, 1–15. https://doi.org/10.1017/jog.2023.70

Martos, Y. M., Catalán, M., Jordan, T. A., Golynsky, A., Golynsky, D., Eagles, G., & Vaughan, D. G. (2017). Heat flux distribution of Antarctica unveiled. *Geophysical Research Letters*, *44*(22), 11417–11426. https://doi.org/10.1002/2017GL075609

Morlighem, M., Rignot, E., Binder, T., Blankenship, D., Drews, R., Eagles, G., et al. (2020). Deep glacial troughs and stabilizing ridges unveiled beneath the margins of the Antarctic ice sheet. *Nature Geoscience*, *13*(2), 132–137. https://doi.org/10.1038/s41561-019-0510-8

Mouginot, J., Rignot, E., & Scheuchl, B. (2019). Continent-wide, interferometric SAR phase, mapping of Antarctic ice velocity. *Geophysical Research Letters*, *46*(16), 9710–9718. https://doi.org/10.1029/2019GL083826

21699011, 2024, 4, Downloaded from https://agupubs.onlinelibrary.wiley.com/doi/10.1029/2023JF007421 by University Of Waterloo Dana Po, Wiley Online Library on [09/08/2024]. See the Terms and Conditions (https://onlinelibrary.wiley.com/terms-and-conditions) on Wiley Online Library for rules of use; OA articles are governed by the applicable Creative Commons License

Nakayama, Y., Cai, C., & Seroussi, H. (2021). Impact of subglacial freshwater discharge on pine island ice shelf. *Geophysical Research Letters*, *48*(18), e2021GL093923. https://doi.org/10.1029/2021GL093923

Pattyn, F. (2010). Antarctic subglacial conditions inferred from a hybrid ice sheet/ice stream model. *Earth and Planetary Science Letters*, *295*(3–4), 451–461. https://doi.org/10.1016/j.epsl.2010.04.025

Pattyn, F., Carter, S. P., & Thoma, M. (2016). Advances in modeling subglacial lakes and their interaction with the Antarctic ice sheet. *Philosophical Transactions of the Royal Society A: Mathematical, Physical and Engineering Sciences*, *374*(2059), 20140296. https://doi.org/10.1098/rsta.2014.0296

Pittard, M. L., Roberts, J. L., Galton-Fenzi, B. K., & Watson, C. S. (2016). Sensitivity of the Lambert-Amery glacial system to geothermal heat flux. *Annals of Glaciology*, *57*(73), 56–68. https://doi.org/10.1017/aog.2016.26

Recinos, B., Goldberg, D., Maddison, J. R., & Todd, J. (2023). A framework for time-dependent ice sheet uncertainty quantification, applied to three west Antarctic ice streams. *The Cryosphere Discussions*, *2023*, 1–46. https://doi.org/10.5194/tc-2023-27

Reese, R., Gudmundsson, G. H., Levermann, A., & Winkelmann, R. (2018). The far reach of ice-shelf thinning in Antarctica. *Nature Climate Change*, *8*(1), 53–57. https://doi.org/10.1038/s41558-017-0020-x

Rignot, E., Jacobs, S., Mouginot, J., & Scheuchl, B. (2013). Ice-shelf melting around Antarctica. *Science*, *341*(6143), 266–270. https://doi.org/10.1126/science.1235798

Rignot, E., Mouginot, J., & Scheuch, B. (2017). *MEaSUREs InSAR-based Antarctica ice velocity map, Version 2*. NASA National Snow and Ice Data Center Distributed Active Archive Center. https://doi.org/10.5067/D7GK8F5J8M8R

Rignot, E., & Steffen, K. (2008). Channelized bottom melting and stability of floating ice shelves. *Geophysical Research Letters*, *35*(2), L02503. https://doi.org/10.1029/2007GL031765

Robin, G. D. Q. (1955). Ice movement and temperature distribution in glaciers and ice sheets. *Journal of Glaciology*, *2*(18), 523–532. https://doi.org/10.3189/002214355793702028

Scambos, T., Fricker, H. A., Liu, C. C., Bohlander, J., Fastook, J., Sargent, A., et al. (2009). Ice shelf disintegration by plate bending and hydro-fracture: Satellite observations and model results of the 2008 Wilkins ice shelf break-ups. *Earth and Planetary Science Letters*, *280*(1–4), 51–60. https://doi.org/10.1016/j.epsl.2008.12.027

Schroeder, D. M., Blankenship, D. D., Raney, R. K., & Grima, C. (2015). Estimating subglacial water geometry using radar bed echo specularity: Application to Thwaites Glacier, West Antarctica. *IEEE Geoscience and Remote Sensing Letters*, *12*(3), 443–447. https://doi.org/10.1109/LGRS.2014.2337878

Schroeder, D. M., Blankenship, D. D., & Young, D. A. (2013). Evidence for a water system transition beneath Thwaites Glacier, West Antarctica. *Proceedings of the National Academy of Sciences of the United States of America*, *110*(30), 12225–12228. https://doi.org/10.1073/pnas.1302828110

Schwanghart, W., & Scherler, D. (2014). Short communication: TopoToolbox 2 - MATLAB-based software for topographic analysis and modeling in Earth surface sciences. *Earth Surface Dynamics*, *2*(1), 1–7. https://doi.org/10.5194/esurf-2-1-2014

Seroussi, H., Ivins, E. R., Wiens, D. A., & Bondzio, J. (2017). Influence of a West Antarctic mantle plume on ice sheet basal conditions. *Journal of Geophysical Research: Solid Earth*, *122*(9), 7127–7155. https://doi.org/10.1002/2017JB014423

Shapiro, N. M., & Ritzwoller, M. H. (2004). Inferring surface heat flux distributions guided by a global seismic model: Particular application to Antarctica. *Earth and Planetary Science Letters*, *223*(1–2), 213–224. https://doi.org/10.1016/j.epsl.2004.04.011

Shen, W., Wiens, D. A., Lloyd, A. J., & Nyblade, A. A. (2020). A geothermal heat flux map of Antarctica empirically constrained by seismic structure. *Geophysical Research Letters*, *47*(14), 1–8. https://doi.org/10.1029/2020GL086955

Shepherd, A., Gilbert, L., Muir, A. S., Konrad, H., McMillan, M., Slater, T., et al. (2019). Trends in Antarctic ice sheet elevation and mass. *Geophysical Research Letters*, *46*(14), 8174–8183. https://doi.org/10.1029/2019GL082182

Shreve, R. L. (1972). Movement of water in glaciers. *Journal of Glaciology*, *11*(62), 205–214. https://doi.org/10.3189/s002214300002219x

Siegfried, M. R., & Fricker, H. A. (2018). Thirteen years of subglacial lake activity in Antarctica from multi-mission satellite altimetry. *Annals of Glaciology*, *59*(76pt1), 42–55. https://doi.org/10.1017/aog.2017.36

Smith, B. E., Fricker, H. A., Gardner, A. S., Medley, B., Nilsson, J., Paolo, F. S., et al. (2020). Pervasive ice sheet mass loss reflects competing ocean and atmosphere processes. *Science*, *368*(6496), 1239–1242. https://doi.org/10.1126/science.aaz5845

Smith, B. E., Fricker, H. A., Joughin, I. R., & Tulaczyk, S. (2009). An inventory of active subglacial lakes in Antarctica detected by ICESat (2003–2008). *Journal of Glaciology*, *55*(192), 573–595. https://doi.org/10.3189/002214309789470879

Smith, B. E., Gourmelen, N., Huth, A., & Joughin, I. (2017). Connected subglacial lake drainage beneath Thwaites Glacier, West Antarctica. *The Cryosphere*, *11*(1), 451–467. https://doi.org/10.5194/tc-11-451-2017

Spergel, J. J., Kingslake, J., Creyts, T., Van Wessem, M., & Fricker, H. A. (2021). Surface meltwater drainage and ponding on Amery ice shelf, East Antarctica, 1973–2019. *Journal of Glaciology*, *67*(266), 1–14. https://doi.org/10.1017/jog.2021.46

Stearns, L. A., Smith, B. E., & Hamilton, G. S. (2008). Increased flow speed on a large east Antarctic outlet glacier caused by subglacial floods. *Nature Geoscience*, *1*(12), 827–831. https://doi.org/10.1038/ngeo356

St-Laurent, P., Yager, P. L., Sherrell, R. M., Stammerjohn, S. E., & Dinniman, M. S. (2017). Pathways and supply of dissolved iron in the Amundsen Sea (Antarctica). *Journal of Geophysical Research: Oceans*, *122*(9), 7135–7162. https://doi.org/10.1002/2017JC013162

Twelves, A. G., Goldberg, D. N., Henley, S. F., Mazloff, M. R., & Jones, D. C. (2021). Self-shading and meltwater spreading control the transition from light to iron limitation in an Antarctic coastal polynya. *Journal of Geophysical Research: Oceans*, *126*(2), 1–28. https://doi.org/10.1029/2020JC016636

Utke, J., Naumann, U., Fagan, M., Tallent, N., Strout, M., Heimbach, P., et al. (2008). OpenAD/F: A modular open-source tool for automatic differentiation of Fortran codes. *ACM Transactions on Mathematical Software*, *34*(4), 1–36. https://doi.org/10.1145/1377596.1377598

Van Liefferinge, B., & Pattyn, F. (2013). Using ice-flow models to evaluate potential sites of million year-old ice in Antarctica. *Climate of the Past*, *9*(5), 2335–2345. https://doi.org/10.5194/cp-9-2335-2013

van Wessem, J. M., van de Berg, W. J., Noël, B. P. Y., van Meijgaard, E., Amory, C., Birnbaum, G., et al. (2018). Modelling the climate and surface mass balance of polar ice sheets using RACMO2 – Part 2: Antarctica (1979–2016). *The Cryosphere*, *12*(4), 1479–1498. https://doi.org/10.5194/tc-12-1479-2018

Wearing, M. G., Hindmarsh, R. C., & Worster, M. G. (2015). Assessment of ice flow dynamics in the zone close to the calving front of Antarctic ice shelves. *Journal of Glaciology*, *61*(230), 1194–1206. https://doi.org/10.3189/2015JoG15J116

Wei, W., Blankenship, D. D., Greenbaum, J. S., Gourmelen, N., Dow, C. F., Richter, T. G., et al. (2020). Getz Ice Shelf melt enhanced by freshwater discharge from beneath the West Antarctic ice sheet. *The Cryosphere*, *14*(4), 1399–1408. https://doi.org/10.5194/tc-14-1399-2020

21699011, 2024, 4, Downloaded from https://agupubs.onlinelibrary.wiley.com/doi/10.1029/2023JF007421 by University Of Waterloo Dana Po, Wiley Online Library on [09/08/2024]. See the Terms and Conditions (https://onlinelibrary.wiley.com/terms-and-conditions) on Wiley Online Library for rules of use; OA articles are governed by the applicable Creative Commons License

Wen, J., Wang, Y., Wang, W., Jezek, K. C., Liu, H., & Allison, I. (2010). Basal melting and freezing under the Amery Ice Shelf, East Antarctica. *Journal of Glaciology*, *56*(195), 81–90. https://doi.org/10.3189/002214310791190820

Werder, M. A., Hewitt, I. J., Schoof, C. G., & Flowers, G. E. (2013). Modeling channelized and distributed subglacial drainage in two dimensions. *Journal of Geophysical Research: Earth Surface*, *118*(4), 2140–2158. https://doi.org/10.1002/jgrf.20146

Wright, A., & Siegert, M. (2012). A fourth inventory of Antarctic subglacial lakes. *Antarctic Science*, *24*(6), 659–664. https://doi.org/10.1017/S095410201200048X

21699011, 2024, 4, Downloaded from https://agupubs.onlinelibrary.wiley.com/doi/10.1029/2023JF007421 by University Of Waterloo Dana Po, Wiley Online Library on [09/08/2024]. See the Terms and Conditions (https://onlinelibrary.wiley.com/terms-and-conditions) on Wiley Online Library for rules of use; OA articles are governed by the applicable Creative Commons License